Chapter 4

PYRRHOTITE MINERALOGY

4.1 Introduction

As described in Chapter 2, a general understanding of the details of pyrrhotite mineralogy already exists, but the majority of the research was focussed on the use of synthetic samples in order to understand pyrrhotite phase relations and determine pyrrhotite crystal structures (Section 2.6.1). Similarly, although the compositional variation and nature of the mineral association between natural samples from a variety of ore deposits have been examined in the past, this was based on the d-spacing method of Arnold and Reichen (1962) and not on direct chemical methods. Therefore the use of mineralogical information based on natural samples using modern mineralogical analysis techniques is of key interest within the field of process mineralogy. In order to be able to develop the relationship between pyrrhotite mineralogy and flotation performance, a thorough characterisation of the mineralogy of pyrrhotite from selected nickel and platinum group element ore deposits is needed. Consequently, the aim of this chapter is *explore and compare the mineralogy in terms of the mineral association, crystallography and mineral chemistry of magnetic and non-magnetic pyrrhotite*. The results of the petrographic, crystallographic and mineral chemistry studies of the various pyrrhotite samples are therefore presented in this chapter. The complete mineral chemistry data set is presented in Appendix A.

4.2 Petrography

Measurement of the relative proportions of non-magnetic and magnetic pyrrhotite in this study using the magnetic colloid method is subject to the interpretation of the textures enhanced by the colloid itself. It is known that particles of the magnetic colloid preferentially adhere to zones where the greatest inhomogeneities exist in the magnetic field and correspond to the occurrence of ferrimagnetic (magnetic) pyrrhotite (Zapletal, 1969). On application of the magnetic colloid onto non-magnetic pyrrhotite or pentlandite, the magnetic colloid particles showed no evidence of preferential attachment and simply hovered homogeneously over the entire ore sample. On repeated application of the magnetic colloid onto a ferrimagnetic pyrrhotite sample, it was found that the exact same textures were enhanced as on the previous occasion. According to Yamamoto *et al.* (1959), only when an external magnetic field is applied to the same sample, do the patterns in the magnetic domains shift slightly, although the boundary between non-magnetic and magnetic phases remains unaltered. In the study of Zapletal (1972), a comparison was made of intergrowths between pyrrhotite phases enhanced by the magnetic colloid method and acid etch technique, the results of which indicated a good correlation. Based on this evidence, the magnetic colloid method was the preferred method used in this study.

4.2.1 Merensky Reef Pyrrhotite

Pyrrhotite samples from the Merensky Reef at Impala Platinum Mine used for mineral characterisation in this study originated from two cross sections through the Merensky Reef. Both of these cross sections sampled the norite footwall, the Merensky chromitite and the overlying pyroxenite giving a reasonable approximation of the variation in lithology within the Merensky Reef in order to examine pyrrhotite mineralogy in detail (Figure 3.1). In hand, specimen the two samples differed most notably in the coarser-grained, more pegmatoidal textured pyroxenite overlying the Merensky chromitite in sample *IMP-1*, relative to sample *IMP-2*.

Overview of sulfide mineralogy

Sulfide mineralization within the Merensky reef samples examined was recognised in three textural settings as follows:

i) Large multi-mineralic sulfide blebs or domains
ii) Smaller mono-mineralic sulfide blebs
iii) Disseminated sulfides

The first texture comprising multi-mineralic sulfide blebs consisted of irregularly shaped domains of sulfides interstitial to the coarser grained, cumulus orthopyroxene. These sulfide blebs could be up to several millimetres in size and were comprised of the minerals pyrrhotite, pentlandite and chalcopyrite. These sulfide blebs were variable in texture and commonly consisted of a core of pyrrhotite surrounded by a rim of granular pentlandite and chalcopyrite (Figure 4.1a, b). Alternatively, equigranular mosaic textured domains were also recognised.

The second sulfide texture observed consisted of fine grained sulfide blebs (50 µm), that were still interstitial to the coarse grained silicates but the sulfide blebs were mono-mineralic; with pyrrhotite as the predominant mineral type (Figure 4.1c). The third typical sulfide texture observed within the samples analysed in this study consisted of very fine-grained disseminated sulfides (< 5 µm) which could be hosted by the silicate minerals themselves, or were sometimes restricted to cleavage planes and fracture zones within the silicates. Most of the discrete disseminated sulfide grains were chalcopyrite and were likely to be secondary in origin. The occasional fine-grained (50 µm) sulfide was also observed locked within chromite and was probably encapsulated during chromite annealing.

Pyrrhotite

Pyrrhotite was the most abundant sulfide mineral in the Merensky Reef samples analysed and typically occurred as the host phase of other minerals due to the formation of the other base metal sulfide minerals from the MSS (Figure 4.1a, b). Within these large multi-mineralic blebs, pyrrhotite generally consisted of a single large pyrrhotite grain in the core up to a few hundred microns in size, whereas the smaller sulfide blebs consisted of multiple pyrrhotite grains showing well-developed anisotropism. On occasion, it was possible to observe fine lamellar twinning within pyrrhotite.

Treatment of the Merensky samples with the magnetic colloid showed that magnetic pyrrhotite was restricted to sample *IMP-1* (Figure 4.1d, e). Pyrrhotite in sample *IMP-1* consisted of more than ~ 95% magnetic pyrrhotite. The magnetic colloid highlighted a texture

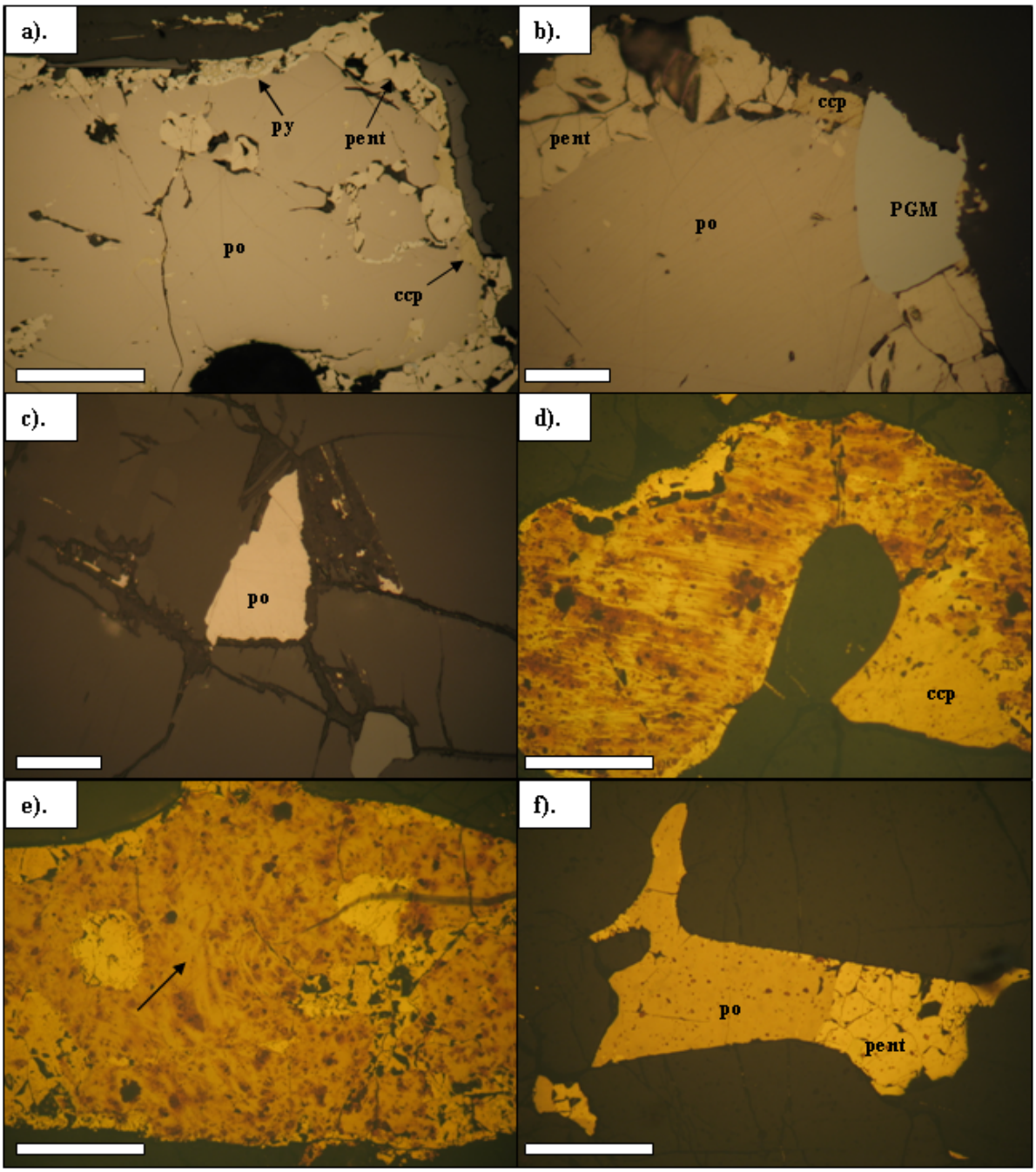

Figure 4.1: Photomicrographs of Impala Merensky Reef pyrrhotite shown in RPL. (a) Multi-mineralic sulfide domain texture consisting of granular pentlandite and chalcopyrite surrounding a core of pyrrhotite. (b) Discrete PGM hosted by a multi-mineralic sulfide domain. (c) Mono-mineralic sulfide bleb consisting of pyrrhotite. (d, e) Magnetic colloid treatment shows sample *IMP-1* consists of almost entirely magnetic pyrrhotite. The arrow in (e) highlights a zone of magnetic pyrrhotite with limited colloid coverage. (f) Magnetic colloid treatment shows non-magnetic pyrrhotite in sample *IMP-2*. Scale bar represents 500 µm for (a, d-f) and 50 µm for (b and c).

of multiple, closely spaced lamellae of magnetic pyrrhotite between 5 and 10 µm in thickness. These lamellae were typically tapered and narrowed towards a point before a new lamella commenced; a feature known as growth zonation (see also Figure 2.12). The length of these individual lamellae varied between 30 and 200 µm in size with the longer length lamellae restricted to larger pyrrhotite grains. In some circumstances the coverage of the colloid on the magnetic pyrrhotite was not entirely homogeneous, a feature which is more likely due to the magnetic domain structure of the pyrrhotite rather than the presence of non-magnetic pyrrhotite (Figure 4.1e).

Non-magnetic pyrrhotite on the other hand was restricted to sample *IMP-2* which was generally more pristine in character (Figure 4.1f). Exsolved troilite hosted by pyrrhotite was also observed in sample *IMP-2*. The troilite occurred as minor exsolution flames with a distinct "zig-zag" like pattern and were generally less than 5 µm in width (Figure 4.2). The direction of troilite exsolution was noted to be parallel to flame pentlandite exsolution, indicating the crystallographic control during exsolution.

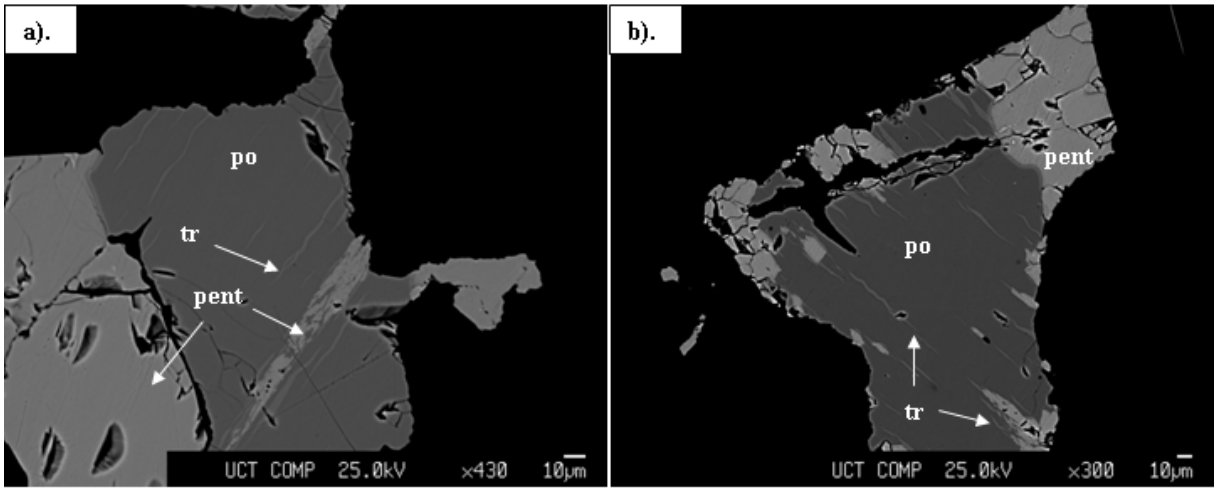

Figure 4.2: Back scattered electron (BSE) images of non-magnetic pyrrhotite in Merensky Reef sample *IMP-2* with exsolution of troilite (medium grey) and pentlandite (light grey). Exsolution lamellae of both troilite and pentlandite are crystallographically controlled.

Pentlandite

Pentlandite typically occurred in two textural occurrences in the Merensky Reef samples, as granular and flame pentlandite. Granular pentlandite was by far the more abundant and only the occasional pentlandite flame was observed. Granular pentlandite occurring along the

boundaries of the multi-mineralic sulfide blebs was typically subhedral in shape (Figure 4.1a, b), varying in size between 20 and 150 µm, whereas pentlandite occurring in the equigranular mosaic textured aggregates of sulfides was between 30 and 40 µm in size. Both pentlandite occurrences exhibited typical triangular pits as cleavage. The mosaic textured aggregates of pentlandite appeared to tarnish relatively rapidly, and consisted of very fine grained inclusions (these were too fine grained to accurately determine the composition with EMP). The mosaic textured, "altered" pentlandite pyrrhotite aggregates were restricted to sample *IMP-1*. Altered pentlandite was not observed in sample *IMP-2*.

Occasional pentlandite flames were observed but it should be mentioned that they were by no means the dominant pentlandite texture within the Merensky samples analysed here. Pentlandite flames were generally 5 µm in width and up to 50 µm in length and hosted by pyrrhotite. Most zones of pentlandite flames were fairly simple in texture, consisting of less than five discrete flames, oriented parallel to one another.

Other Minerals

Chalcopyrite was common within both the multi-mineralic sulfide blebs interstitial to silicates and as disseminated sulfides hosted by silicates. Within the multi-mineralic sulfide blebs granular chalcopyrite was noted to occur on the boundaries of the sulfide blebs in association with granular pentlandite (Figure 4.1a, b). Occasional pyrite was also recognised and was restricted to the sample *IMP-1* and occurred in association with the "altered pentlandite". Relict textures of large cubic pyrite grains (up to 200 µm in size) also occurred, although they appeared to have suffered from extensive resorption. Rare platinum group minerals were observed within the Merensky Reef sulfides and noted for their occurrence in association with the sulfides (generally hosted within the sulfide blebs). Although only larger euhedral PGMs (up to 100 µm in size, Figure 4.1b) were observed in this study, this is not thought to be representative in that many of the smaller fine-grained and very fine-grained PGMs were more than likely overlooked.

4.2.2 Nkomati Pyrrhotite

Overview of sulfide mineralogy

Pyrrhotite samples used for characterisation in this study were sourced from both the Massive Sulfide Body (MSB) and the Main Mineralized Zone (MMZ). Pyrrhotite was the dominant sulfide for both the MSB and MMZ. Selected photomicrographs of pyrrhotite from the MSB and MMZ are shown in figures 4.3 and 4.4, respectively. Four different manifestations of sulfide mineralisation were noted:

(i) Massive sulfide
(ii) Large multi-mineralic sulfide blebs or domains
(iii) Net textured sulfides
(iv) Disseminated sulfides

The MSB was dominated by massive sulphide (texture i), whereas textures (ii) to (iv) were more common within the two MMZ samples analysed (sample *MMZ-1*, *MMZ-4*). Sample *MMZ-1* tended to be the more pristine sample with less sulfide mineralisation which was confined to the development of discrete multi-mineralic sulfide blebs (up to several mm in size and dominated by pyrrhotite; Figure 4.4a) with occasional disseminated sulfides hosted by silicates. Sulfide mineralisation in sample *MMZ-4* however, suggested more interaction of the sulfide melt with the silicate minerals. Mineralisation in sample *MMZ-4* occurred as both domains of massive sulfide and net textured sulfides hosting silicate minerals (Figure 4.4b). These net textured domains appeared to be the result of the resorption of the primary silicate minerals and consequent formation of acicular tremolite and secondary alteration minerals (e.g. serpentine) surrounding a sulfide core of fine-grained pyrrhotite and pentlandite (Figure 4.4b). The abundance of tremolite in sample *MMZ-4* produced very irregular boundaries between the silicate and sulfide phase due to its acicular nature.

Nkomati MSB Pyrrhotite

Pyrrhotite

Pyrrhotite was the dominant sulfide in the MSB ore and generally occurred as subhedral shaped grains between 200 and 1000 µm in size, with an average of ~ 400 µm (Figure 4.3a).

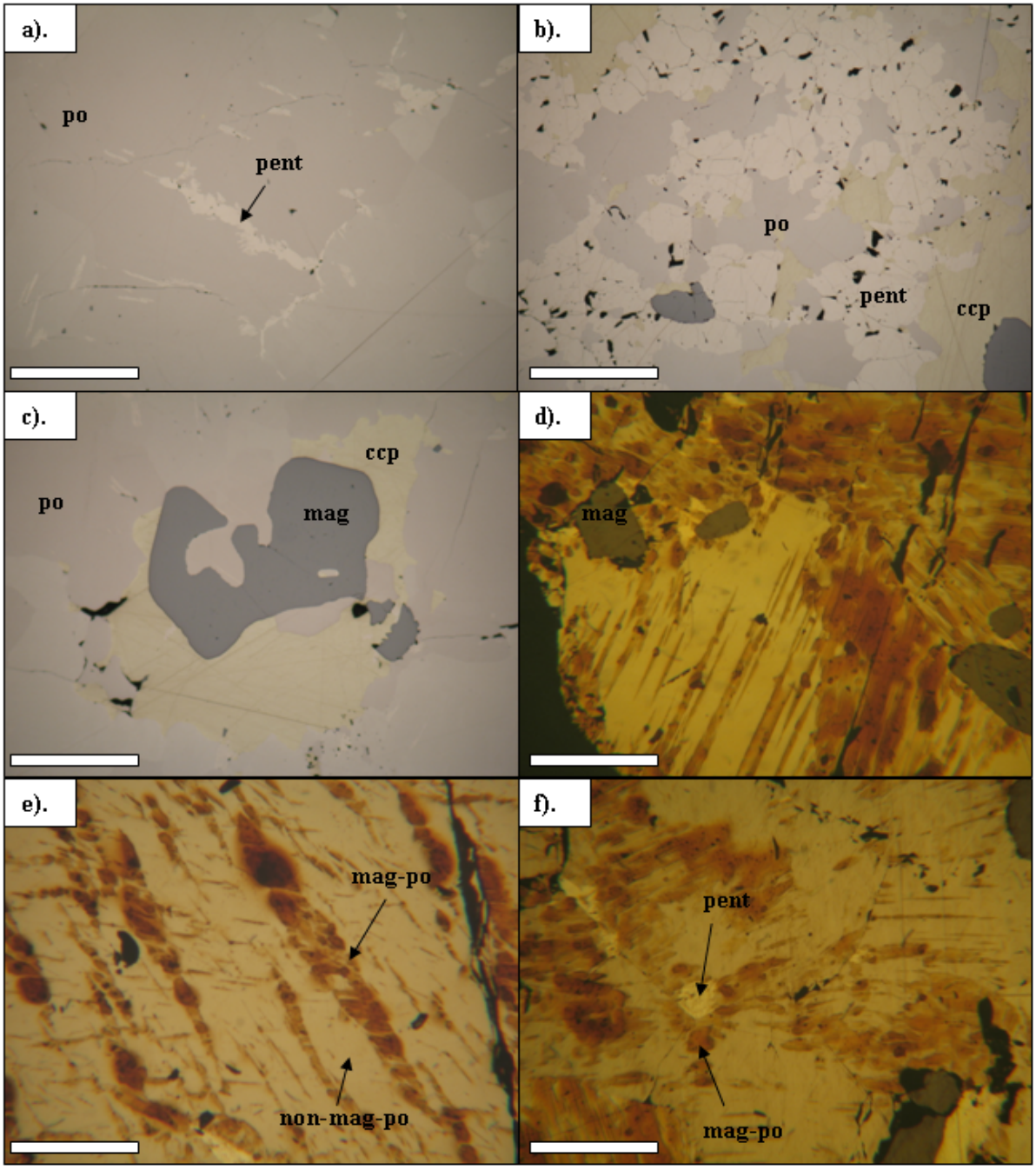

Figure 4.3: Photomicrographs of the Nkomati MSB shown in RPL. (a) Coarse-grained pyrrhotite hosting flame pentlandite inclusions. (b) Aggregate of granular pentlandite intergrown with pyrrhotite and chalcopyrite. (c) Irregular shaped inclusion of magnetite and chalcopyrite hosted by pyrrhotite. (d) Magnetic colloid treatment shows lamellae of magnetic pyrrhotite hosted by non-magnetic pyrrhotite. (e) Magnetic colloid treatment shows composite lamellae of magnetic pyrrhotite hosted by non-magnetic pyrrhotite. (f) Magnetic colloid treatment shows magnetic pyrrhotite rims surrounding flame pentlandite. Scale bar represents 200 µm.

Pyrrhotite grains in contact with other sulfides e.g. pentlandite, could however have more irregular shaped grain boundaries (Figure 4.3b, c). Since pyrrhotite formed from the host MSS (Section 2.2.7) in the Nkomati MSB ore, it contained multiple inclusions of pentlandite, chalcopyrite and also magnetite similar to those shown in figures 4.3 b and c.

Application of the magnetic colloid to the Nkomati MSB pyrrhotite, revealed complex intergrowths of magnetic and non-magnetic pyrrhotite similar to the textures described from the literature (see Figure 2.12). Magnetic pyrrhotite generally occurred as elongate lamellae that were hosted by the non-magnetic phase. Individual magnetic pyrrhotite lamellae could extend up to 50 µm in length. Examples of composite lamellae, thickness zonation, box work textures and formation of magnetic pyrrhotite rims surrounding flame pentlandite were all observed although only photomicrographs of selected intergrowth textures are shown in figure 4.3 e-f. Similar intergrowths of magnetic and non-magnetic pyrrhotite were obtained from the BSE and QEMSCAN images of the Nkomati pyrrhotite in section 3.3 (Figure 3.6).

Pentlandite

Photomicrographs of both the granular and flame pentlandite varieties present in the Nkomati MSB pyrrhotite are shown in figures 4.3a and b. Subhedral granular pentlandite was observed on pyrrhotite grain boundaries and varied between 50 and 150 µm in size. Aggregations of granular pentlandite were sometimes associated with irregular shaped chalcopyrite grains. Exsolved flame pentlandite was relatively abundant along pyrrhotite grain boundaries and fractures. Individual flames were typically 5 µm wide and 30 µm in length and some very intricate feather-like textures were observed. Individual pentlandite flames were also mantled by magnetic pyrrhotite as shown in figure 4.3f. Pentlandite appeared to be relatively unaltered and the violarite described by van Zyl (1996) was not noted here.

Other Minerals

Chalcopyrite and pyrite were both relatively common in the Nkomati MSB pyrrhotite. Chalcopyrite grains were typically irregular in shape and associated with aggregations of granular pentlandite or magnetite (Figure 4.3b, c). Pyrite grains were euhedral with a well developed cubic habit and varied in size by several orders of magnitude (e.g. from 50 to 5000 µm). Magnetite was also relatively abundant and formed anhedral grains which varied from rounded to elongate (Figure 4.3c). Variable degrees of ilmenite exsolution forming very fine

grained exsolution lamellae less than 10 µm in size and hosted by magnetite were also observed.

Nkomati MMZ Pyrrhotite

Pyrrhotite

The occurrence of pyrrhotite in the two Nkomati MMZ samples was quite distinct from one another although both contained large sulfide blebs with pyrrhotite occurring as the dominant host phase from the MSS (Figure 4.4a-d). In sample *MMZ-1* pyrrhotite occurred in discrete sulfide blebs and individual grains that were up to 1 mm in size. Pyrrhotite in both samples appeared to show a very distinct parting developed parallel to the direction of flame pentlandite exsolution, but closer examination revealed the "parting" was in fact very fine-grained elongate rod-like inclusions of magnetite (30 µm in length, 2 µm in width; Figure 4.4c). The fine-grained magnetite inclusions suggest that the MSS must have contained some dissolved oxygen upon cooling and crystallisation of pyrrhotite. These magnetite inclusions were more common in sample *MMZ-1* than *MMZ-4*, whereas the occurrence of magnetite as larger anhedral grains (up to 200 µm in size) hosted by pyrrhotite was restricted to sample *MMZ-4* (Figure 4.4d). The individual grain size of pyrrhotite in sample *MMZ-4* was also slightly smaller (100-200 µm) relative to sample *MMZ-1*.

Treatment of pyrrhotite with the magnetic colloid revealed that sample *MMZ-1* was entirely magnetic (Figure 4.4e), whereas sample *MMZ-4* consisted of inter-grown magnetic and non-magnetic pyrrhotite (Figure 4.4f) more similar to the pyrrhotite from the MSB (Figure 4.3d-f). Individual lamellae of magnetic pyrrhotite in sample *MMZ-1* were up to 100 µm in length and 10 µm in width. These lamellae were always parallel to one another within a grain and also showed thickness zonation (see also Figure 2.12). Magnetic pyrrhotite lamellae in sample *MMZ-4* tended to be smaller (50 µm in length, < 10 µm in width) and sparser and typically hosted by the non-magnetic phase (Figure 4.4f). Concentrations of magnetic pyrrhotite were also observed on pyrrhotite grain boundaries. The relative proportion of magnetic to non-magnetic pyrrhotite in sample *MMZ-4* tended to be quite variable with some domains dominated by magnetic pyrrhotite and vice versa.

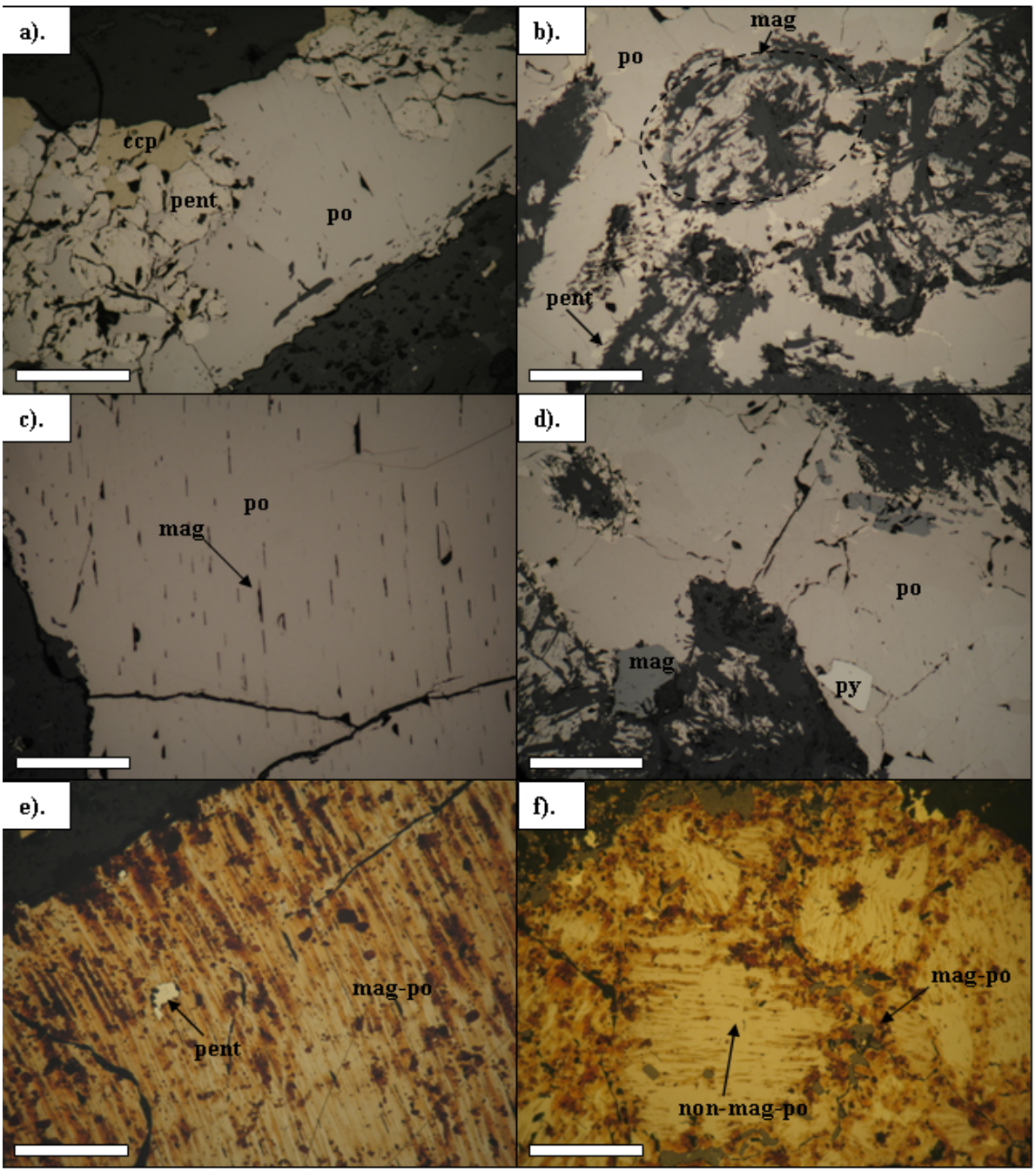

Figure 4.4: Photomicrographs of the Nkomati Main Mineralised Zone (MMZ) pyrrhotite shown in RPL. (a) Typical sulfide bleb of chalcopyrite and pentlandite with pyrrhotite as the host phase in sample *MMZ-1*. (b) Net textured sulfide intergrown with acicular tremolite from sample *MMZ-4*. See marked ellipse highlighting the outline of a relict silicate. (c) Very fine-grained magnetite inclusions hosted by pyrrhotite in sample *MMZ-1*. (d) Net texture pyrrhotite with anhedral magnetite and subhedral pyrite in sample *MMZ-1*. (e) Magnetic colloid treatment shows sample *MMZ-1* is entirely magnetic pyrrhotite. Note the thickness zonation evident in the magnetic pyrrhotite lamellae. (f) Magnetic colloid treatment shows intergrowths of both magnetic and non-magnetic pyrrhotite in sample *MMZ-4.* Scale bar represents 200µm.

Pentlandite

Pentlandite commonly occurred as granular pentlandite that was developed along the margins of the multi-mineralic sulfide domains and net textured sulfide blebs (Figure 4.4a, b). Individual grains were ~ 200 µm in size and showed well-developed octahedral cleavage. Granular pentlandite tended to have an irregular pock marked texture which was previously described by van Zyl (1996) as due to the development of very fine-grained violarite inclusions. Pentlandite flames up to 30 µm in length and less than 5 µm in width also occurred, but were fairly sparse in both MMZ samples.

Other Minerals

Chalcopyrite was noted in both samples of MMZ ore examined and occurred as large euhedral grains (300 µm) associated with the boundary of the large sulfide domains (Figure 4.4a) and also as very fine-grained monomineralic inclusions (< 50 µm) hosted by the silicate minerals. Pyrite was recognised in both occurrences of pyrrhotite examined in the MMZ ore, but was more common for sample *MMZ-4* where it occurred as medium-grained euhedral to subhedral grains hosted by pyrrhotite (Figure 4.4d). Pyrite in sample *MMZ-1* more commonly occurred as fine-grained lenses less than 10 µm in width forming partial rims to the sulfide domains. Magnetite was also recognised in two different morphologies. The first of which was discrete magnetite grains and the second, very fine-grained inclusions in pyrrhotite forming parallel rods situated in the same direction as the pentlandite flame exsolution suggesting that their formation was crystallographically controlled (Figure 4.4c). Both occurrences of magnetite were recognised in sample *MMZ-4*, whereas in *MMZ-1* only the very fine-grained magnetite was recognised. Some oxy-exsolution of ilmenite from magnetite was recognised in the larger anhedral magnetite grains from pyrrhotite sample *MMZ-4*.

4.2.3 Phoenix Pyrrhotite

Pyrrhotite samples sourced from the Phoenix ore deposit in this study were generally massive in nature although they contained some irregular shaped, millimetre sized silicate inclusions. Sulfide minerals hosted by the silicate inclusions tended to be fairly resorbed (Figure 4.5a). The Phoenix ore was fairly heavily fractured and dominated by pyrrhotite as the host sulfide with abundant flame pentlandite, lesser chalcopyrite and pyrite.

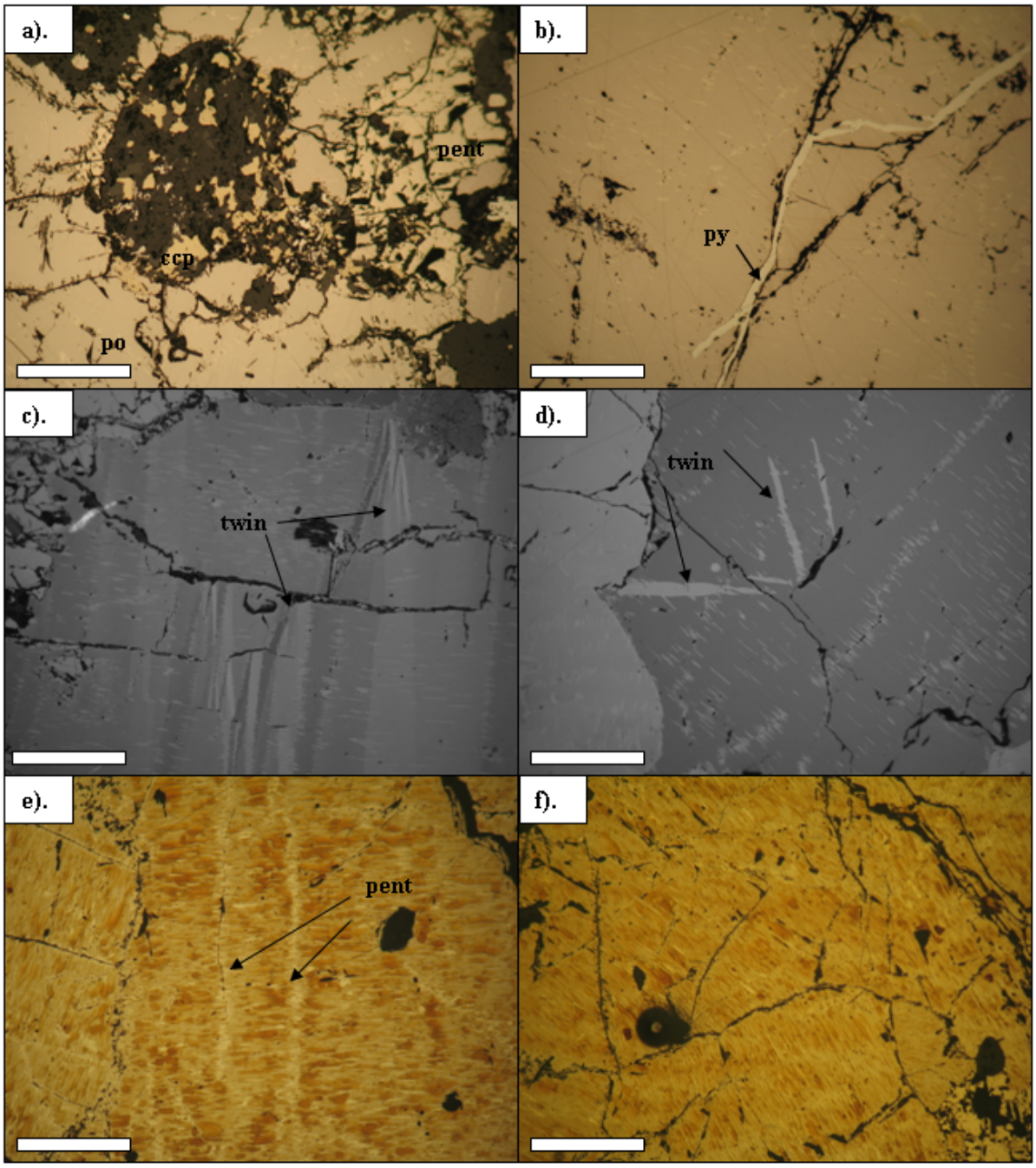

Figure 4.5: Photomicrographs of the Phoenix massive sulfide ore shown in RPL and XPRL (c, d). (a) Silicate inclusion hosted by the massive sulfide. Note the resorbed nature of the pyrrhotite hosting the silicate inclusion. (b) Pyrite vein hosted by pyrrhotite, which in turn hosts multiple flame pentlandite lamellae. (c, d) Twinning in pyrrhotite. Feathered textures belong to the flame pentlandite lamellae. (e, f) Magnetic colloid treatment shows Phoenix pyrrhotite is magnetic. Note the exsolution of flame pentlandite parallel from a fracture, coincident to the direction of magnetic pyrrhotite lamellae in (e). Scale bar represents 200 µm.

Pyrrhotite

Pyrrhotite occurred as large, well-developed grains up to a few millimetres in size although grain boundaries were marked by extensive fracturing (Figure 4.5a, b). The grains showed limited variation in size in the massive sulfide ore whereas for pyrrhotite hosted by silicate inclusions, individual grains were as small as 100 µm. Pyrrhotite grains hosted by silicate inclusions showed extensive resorption on grain boundaries (Figure 4.5a). Occasional twinning was also visible as discrete elongate lamellae up to 200 µm long and 30 µm wide from which pentlandite flame exsolution occurred (Figure 4.5 c, d, see also Figure 2.12).

Use of the magnetic colloid method illustrated that Phoenix pyrrhotite was entirely magnetic with no evidence of the non-magnetic pyrrhotite phase (Figure 4.5e, f). Individual magnetic pyrrhotite lamellae highlighted by the use of the colloid were always parallel to one another within a single grain. Sometimes the magnetic pyrrhotite lamellae were truncated by a perpendicularly running feature (e.g. twin boundary, grain boundary or fracture) from which abundant pentlandite flame exsolution occurred, parallel to the direction of the magnetic pyrrhotite lamellae (Figure 4.5e).

Pentlandite

Pentlandite commonly occurred in two textural settings, with the third only occurring occasionally. Pentlandite in the Phoenix deposit was encountered as large mosaic textured, granular pentlandite domains up to several millimetres in size. Individual grains of granular pentlandite were 100 to 200 µm in size, and showed parting as well as well-developed triangular pits indicative of their cubic cleavage (Figure 4.5a). The second and far more common occurrence of pentlandite was exsolved flame pentlandite lamellae hosted by pyrrhotite (Figure 4.5b). These “featherlike” flames, less than 5 µm in width but up to 30 µm in length were always parallel to one another, confirming the crystallographic control during the exsolution process. Pentlandite flames were recognised as exsolution lamellae from pyrrhotite grain boundaries, fractures and twin planes. Granular pentlandite was subtly more yellow than the cream flame pentlandite. A third and more minor occurrence of pentlandite consisted of granular pentlandite veins linking mosaic textured pentlandite domains to one another across the ore sample and which typically occurred in association with pyrite.

Other Minerals

Chalcopyrite was generally fairly sparse in the massive samples examined and where observed, occurred in association with granular pentlandite domains or pyrite veins. Some coarse grained chalcopyrite was however, recognised within the silicate inclusions. Unlike pyrrhotite hosted by the silicate inclusions, the chalcopyrite showed no indication of extensive resorption. Pyrite commonly occurred as irregular shaped veins cross cutting the pyrrhotite (Figure 4.5b). These veins varied in width between 20 and 60 µm and appeared to show no distinct grain boundaries. Within the pyrite veins, occasional inclusions hosting very fine grained anhedral sphalerite (< 10 µm) were also observed. Pyrite hosted by the silicate inclusions was very dissimilar to that in the massive sulfide, since euhedral pyrite cubes (50 µm) were recognised in conjunction with other finer grained resorbed spherules of pyrite.

4.2.4 Sudbury Pyrrhotite

Overview of sulfide mineralogy

Sulfide mineralization from the Copper Cliff North (Figure 4.6), and Gertrude and Gertrude West pyrrhotite samples (Figure 4.7, 4.8) from Sudbury examined in this study occurred in two textural settings as follows:

i) Massive sulfide to semi-massive sulfides
ii) Disseminated sulfides

The first texture comprising massive sulfide was the dominant texture in the Copper Cliff North and Gertrude West ores (Figure 4.7a), whereas the Gertrude pyrrhotite tended to be massive to semi-massive. All three ores contained silicate inclusions of several millimetres in size and which hosted disseminated sulfides. The disseminated sulfides were mostly comprised of pyrrhotite although occasional chalcopyrite was present. Pyrrhotite hosted by silicate inclusions was generally irregular in shape and varied in size from 50 µm (Copper Cliff North) to 200 µm (Gertrude).

Sudbury Copper Cliff North (CCN) Pyrrhotite

Pyrrhotite

Pyrrhotite occurred in three textural forms within the massive sulfide ore. The first consisted of coarse-grained, well-developed euhedral pyrrhotite grains up to 2 mm in size showing perpendicular partings (Figure 4.6a). The second textural form consisted of medium-grained aggregations of pyrrhotite grains on the order of 200 µm in size. The third textural form occurred as finely disseminated pyrrhotite grains hosted by silicate inclusions. Examination of coarse-grained pyrrhotite showed that the seemingly homogeneous pyrrhotite showed the development of several varieties of twinning including discrete lamellae (up to 200 µm in length and 50 µm in width) and also more irregular shaped twins (Figure 4.6b).

Pyrrhotite was dominated by the non-magnetic phase with occasional magnetic pyrrhotite lamellae (< 5 %) present at the grain boundaries of pentlandite in all the textural forms of its occurrence (Figure 4.6c, d). Although the morphology of the magnetic pyrrhotite was not always well defined by the colloid, some discrete lamellae 20-30 µm radiating from the pentlandite grain boundaries could be recognised.

Pentlandite

Pentlandite occurred in three textural relationships in the Sudbury CCN pyrrhotite. The first and most common textural relationship consisted of granular pentlandite showing well-developed octahedral cleavage. This granular pentlandite had a distinctive brecciated appearance and consisted of many individual grains (up 250 µm in size) forming a pentlandite aggregate several millimetres in size. The second textural occurrence comprised granular pentlandite "veins" on pyrrhotite grain boundaries (Figure 4.6a, d), with individual pentlandite grains between 50 and 100 µm in size. Occasional chalcopyrite grains 10-20 µm in size were associated with the pentlandite veins. The third textural occurrence of pentlandite was caused by pentlandite exsolution from the granular veins, resulting in the formation of finely developed flames of pentlandite that extended in excess of 30 µm away from pentlandite granular veins. Pentlandite flames which exsolved from fractures and grain boundaries within the pyrrhotite MSS were generally rather rare, although when present were noted to display intricate feather-like textures and were free from fracturing unlike vein and granular pentlandite.

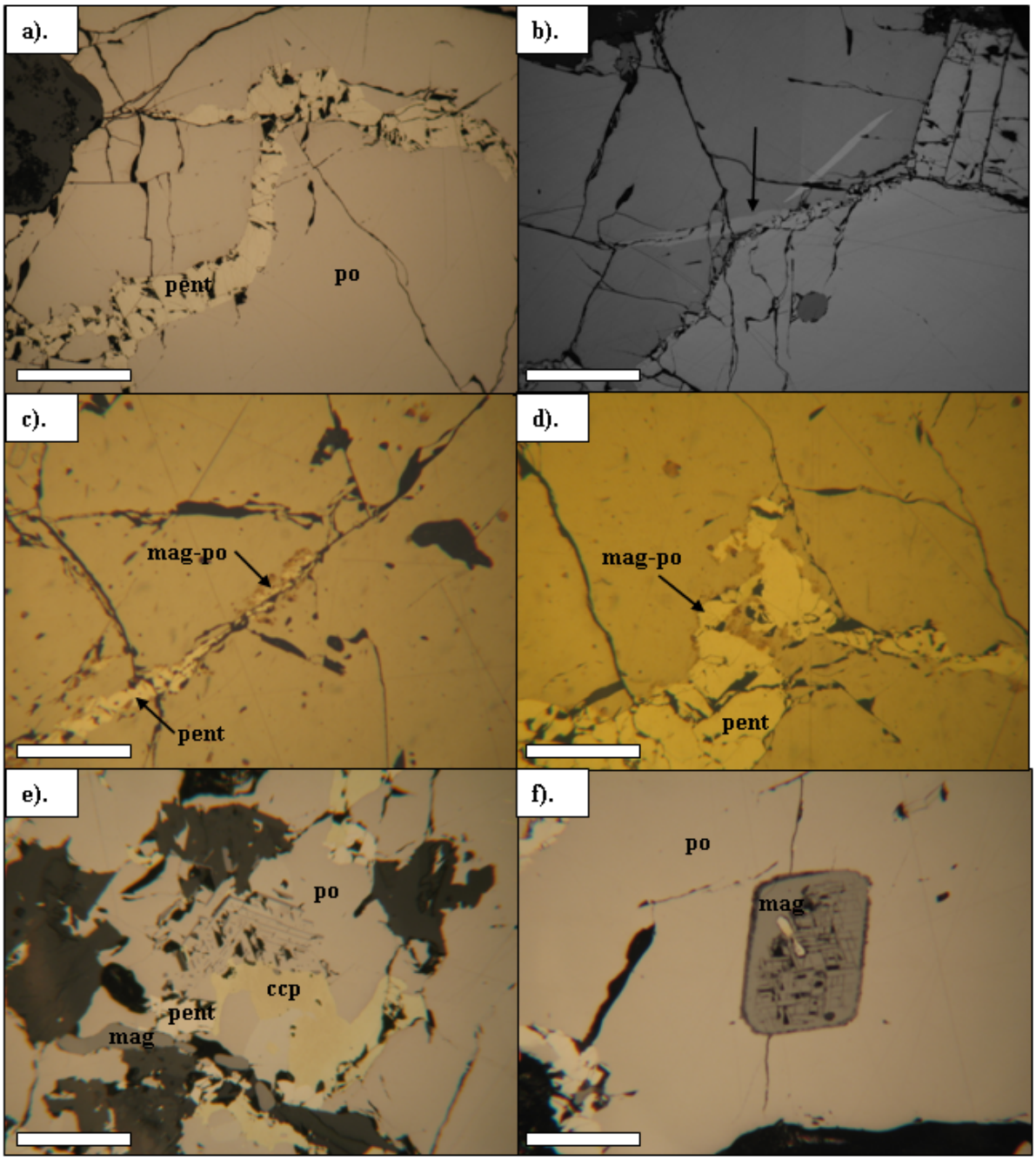

Figure 4.6: Photomicrographs of Sudbury Copper Cliff North ore shown in RPL and XPRL (b). (a) Massive sulfide texture with pyrrhotite as the host phase. Pyrrhotite grain boundaries are intersected by veins of granular pentlandite. (b) Twinning in pyrrhotite, shown in XPL. (c) Magnetic colloid treatment shows non-magnetic pyrrhotite hosting a vein of fine-grained pentlandite mantled by a thin rim of magnetic pyrrhotite. (d) Magnetic colloid treatment shows non-magnetic pyrrhotite hosting granular pentlandite mantled by a thin rim of magnetic pyrrhotite. (e) Intergrowth of magnetite, pentlandite, chalcopyrite and pyrrhotite. (f) Euhedral titanomagnetite grain with cross cutting exsolved lamellae of ilmenite. The titanomagnetite grain is also mantled by ilmenite. Scale bar represents 200 µm for all photomicrographs.

Other Minerals

Chalcopyrite occurred as individual chalcopyrite grains up to 50 µm in size that were hosted by both pentlandite and pyrrhotite (Figure 4.6e). The chalcopyrite grains were recognised in association with granular pentlandite veins and also the more brecciated granular pentlandite domains. Where chalcopyrite occurred in association with granular pentlandite domains, the individual grains were as large as 400 µm.

Individual magnetite grains were fairly variable in their shape occurring as well developed euhedral crystals with octahedral cleavage (400-500 µm) to extensively resorbed grains consisting of multiple magnetite lamellae (Figure 4.6e, f). Magnetite grains showed octahedrally exsolved lamellae of ilmenite up to 100 µm in length and less than 5 µm in width, orientated at 120^0 to each other (Figure 4.6f). The abundant oxy-exsolution of ilmenite from magnetite here suggested that was relatively titaniferous in composition. These magnetite grains were sometimes rimmed by a combination of ilmenite and another dark mineral which Naldrett and Kullerud (1967) suggested was hercynite.

No pyrite was recognised in any of the Copper Cliff North pyrrhotite samples examined here even though a thorough search was made for it. Occasional small euhedral grains hosted by pyrrhotite with high reflectivity were also observed and may represent one of the accessory phases such as the sulphoarsenides or platinum group minerals recognised in other studies of the Sudbury ores (e.g. Naldrett and Kullerud, 1967; Magyarosi *et al.*, 2002; Szentpéteri *et al.*, 2002).

Sudbury Gertrude and Gertrude West Pyrrhotite

Pyrrhotite

The overall occurrence of pyrrhotite in the Gertrude and Gertrude West samples was similar to Copper Cliff North pyrrhotite, consisting of coarse-grained, medium-grained and fine-grained pyrrhotite occurrences (Figure 4.7, 4.8). The fine-grained pyrrhotite occurrences were more common in the Gertrude sample given its semi-massive nature (Figure 4.7a). These fine-grained pyrrhotite silicate intergrowths generally consisted of fine-grained (30 µm) euhedral crystal growths and formed the gradational boundary between the silicate inclusions and sulfide matrix (Figure 4.7a).

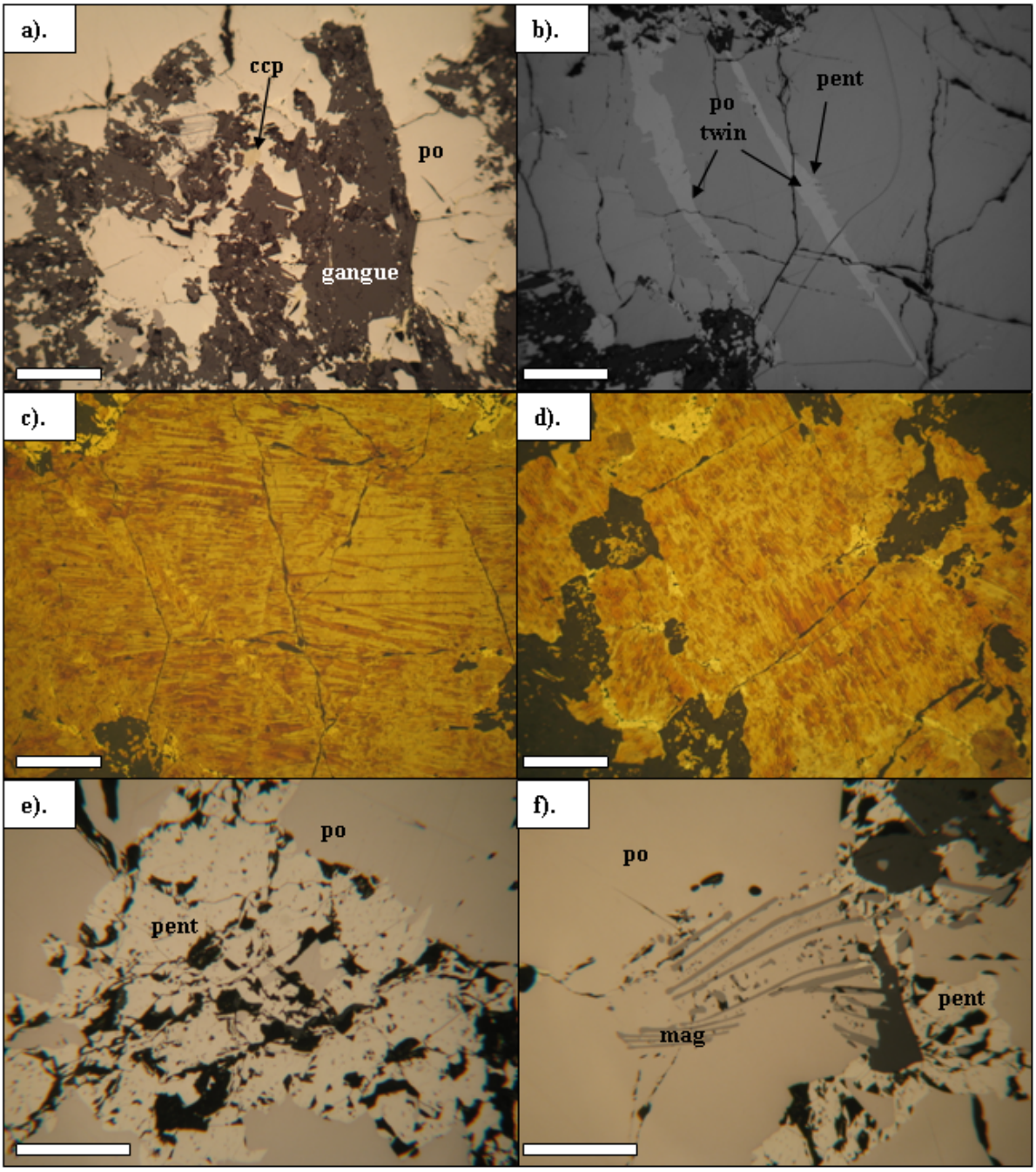

Figure 4.7: Photomicrographs of Sudbury Gertrude pyrrhotite shown in RPL and XPRL (b). (a) Irregular shaped boundaries between semi-massive sulfides and silicate inclusions. (b) Twinning in coarse grained pyrrhotite shown in XPL. Note the flame pentlandite exsolved from the twin boundaries. (c ,d) Magnetic colloid treatment shows Gertrude pyrrhotite is almost entirely magnetic pyrrhotite. (e) Granular pentlandite domains with characteristic "pockmarked" texture due to very fine-grained pyrite inclusions. (f) Extensively resorbed titanomagnetite hosted by pyrrhotite. Scale bar represents 200 µm in (e, f) and 500 µm for the rest.

Gertrude West pyrrhotite was characterised by a well-developed parting (Figure 4.8a), which although present in the Gertrude pyrrhotite was not as well defined. Other internal features recognised in the Gertrude and Gertrude West pyrrhotite samples included the abundance of twinning and exsolution of flame pentlandite from pyrrhotite twin boundaries (Figure 4.7b). Some of the lamellar twins were observed to cross cut grain boundaries and were up to 2 mm in length.

Both the Gertrude and Gertrude West pyrrhotite samples were dominated by the magnetic pyrrhotite phase that showed multiple lamellae with distinctive thickness zonation features (Figure 4.7c, d; 4.8b, c). Other textural features noted with the magnetic colloid included composite lamellae (multiple generations of lamellae located at 60^0 to one another) and box work textures (see Figure 2.12). In some areas, the magnetic colloid did not appear to cover all the pyrrhotite, suggesting that a minor component of non-magnetic pyrrhotite could exist (Figure 4.7c).

Pentlandite

The occurrence of pentlandite in the Gertrude and Gertrude West ores was similar to Copper Cliff North ore since pentlandite occurred in brecciated granular pentlandite domains, granular pentlandite veins and as flame pentlandite. The only notable difference in pentlandite between the ores was the occurrence of a “pockmarked” texture in the granular pentlandite domains and veins (Figure 4.7e, 4.8d), whereas the flame pentlandite was free from this alteration. Closer examination of the pockmarks revealed very fine grained, subhedral pyrite inclusions less than 10 μm in size that were confirmed with EMP analysis.

Other Minerals

Chalcopyrite was fairly sparse in the Gertrude and Gertrude West pyrrhotite samples and where present occurred as irregular shaped blebs in association with granular pentlandite domains or veins. The chalcopyrite was fairly dark yellow in colour possibly due to the presence of very fine grained anisotropic lathes (< 10 μm) which could possibly represent cubanite. Chalcopyrite was also recognised inter-grown with silicate gangue (Figure 4.7a).

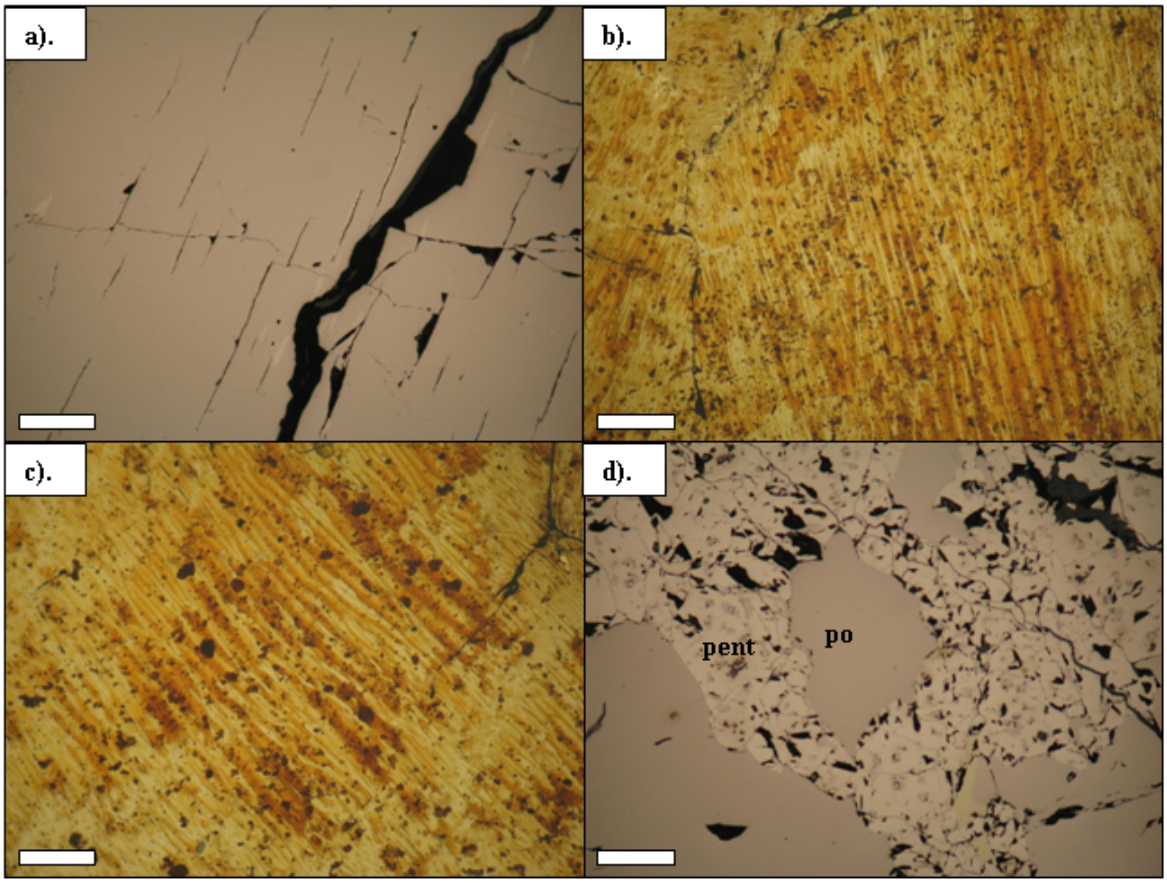

Figure 4.8: Photomicrographs of Sudbury Gertrude West pyrrhotite shown in RPL. (a) Parting developed in coarse-grained pyrrhotite. (b, c) Magnetic colloid treatment shows Gertrude West pyrrhotite is entirely magnetic. (d) Granular pentlandite domains with characteristic "pockmarked" texture caused by very fine-grained pyrite inclusions. Scale bar represents 200 µm.

Titanomagnetite in association with lamellae of ilmenite exsolved by oxy-exsolution were common. Titanomagnetite occurred as anhedral grains 50 to 100 µm in size or as extensively resorbed lamellae of titanomagnetite hosted by pyrrhotite (Figure 4.7f). No discrete ilmenite grains were observed.

Occasional small euhedral grains hosted by pyrrhotite with high reflectivity were also observed and could represent one of the accessory phases such as the sulphoarsenides or platinum group minerals recognised in other studies of the Sudbury ores (e.g. Naldrett and Kullerud, 1967; Magyarosi *et al.*, 2002; Szentpéteri *et al.*, 2002).

4.3 Crystallography

In order to investigate the crystallographic properties of the pyrrhotite samples from nickel and platinum group element ore deposits forming part of this study, pyrrhotite single crystal specimens were analysed by single crystal x-ray diffraction (Section 3.2.3). The aim of the crystallographic studies was primarily to determine the crystallography and unit cell dimensions (Section 1.4) from which the pyrrhotite superstructure could be deduced. The results obtained from the single crystal XRD of the pyrrhotite crystals are shown in table 4.1 along with selected pyrrhotite cell dimensions from the literature. The selection of pyrrhotite single crystals with well-developed crystallinity and without any evidence of twinning was limited to the Impala Merensky Reef (sample *IMP-1*), Phoenix and Sudbury CCN pyrrhotite samples. The complete structure solutions for the Impala Merensky Reef pyrrhotite (sample *IMP-1*) and the Sudbury CCN pyrrhotite can be found in De Villiers *et al.* (In Prep) and De Villiers *et al.* (Submitted).

Table 4.1: Summary of the cell parameters obtained for pyrrhotite single crystals in this study (Impala Merensky Reef sample *IMP-1*, Phoenix, Sudbury CCN pyrrhotite). Comparative cell dimensions from the literature are also shown. [1] This study [2] De Villiers *et al.* (In Prep) [3] Tokonami *et al.* (1972) [4] Powell *et al.* (2004) [5] De Villiers *et al.* (Submitted) [6]Morimoto *et al.* (1975b).

Type	4C Magnetic	4C Magnetic	4C Magnetic	4C Magnetic	5C Non-mag	5C Non-mag
Composition	Fe_7S_8	Fe_7S_8	Fe_7S_8	Fe_7S_8	Fe_9S_{10}	Fe_9S_{10}
Crystallography	Monoclinic	Monoclinic	Monoclinic	Monoclinic	Ortho.	Ortho.
Symmetry	C2	-	F2/d	C2/c	Cmca	C*ca
a (Å)	11.890	11.866	11.902	11.926	6.893	6.885
b (Å)	6.872	6.851	6.859	6.882	11.939	11.936
c (Å)	22.785	22.710	22.787	12.925	28.673	28.676
β	90.12^0	90.08^0	90.26^0	118.02^0	-	-
Location	Impala Merensky	Tati Phoenix	Kisbanya, Romania	Synthetic	Sudbury CCN	Kishu, Japan
References	1, 2	1	3	4	1, 5	6

4.3.1 Merensky Reef Pyrrhotite

Use of the magnetic colloid on pyrrhotite samples in Section 4.2 showed that the Impala Merensky Reef sample *IMP-1* pyrrhotite was magnetic. According to the cell dimensions obtained by single crystal x-ray diffraction as shown in table 4.1, the length of the c-axis for the Merensky pyrrhotite was 22.785 Å, which is approximately four times the length of the NiAs unit cell (5.880 Å; Wyckoff, 1963). Therefore, the Merensky pyrrhotite can be classified as 4C magnetic pyrrhotite. The single crystal x-ray diffraction showed monoclinic symmetry in space group C2 for sample *IMP-1*. Table 4.1 also shows that the cell dimensions obtained for the Merensky pyrrhotite were in good agreement with the 4C pyrrhotite analysed by Tokonami *et al.* (1972) using the unconventional F2/d space group (Figure 2.9).

According to the preliminary crystal structure solution obtained by De Villiers *et al.* (In Prep), the theoretical composition of sample *IMP-1* was $Fe_{6.83}S_8$, and which is slightly more iron deficient than the stoichiometric composition Fe_7S_8 used by Tokonami *et al.* (1972) and Powell *et al.* (2004). This deviation from the ideal composition is most likely due to the non-stoichiometry which is invariably present in natural pyrrhotite samples.

It is apparent from the powder XRD diffractogram shown in figure 4.9a that the Impala Merensky sample *IMP-1* pyrrhotite showed the characteristic doublet for magnetic, monoclinic 4C pyrrhotite similar to that described in Section 2.2.8 and shown in figure 2.14. The d-spacing obtained for the characteristic monoclinic pyrrhotite doublet was ~ 2.052 and 2.062 Å respectively, which shows reasonable correlation to the ideal spacing derived from the structure of Powell *et al.* (2004) of 2.056 and 2.066 Å.

4.3.2 Phoenix Pyrrhotite

Use of the magnetic colloid in Section 4.2 on the Phoenix pyrrhotite showed that it was magnetic and therefore most likely 4C monoclinic pyrrhotite. Single crystal XRD of the Phoenix pyrrhotite sample showed monoclinic symmetry and that the length of the c-axis was 22.710 Å (Table 4.1). This is similar to that obtained for both the Impala Merensky Reef sample *IMP-1* pyrrhotite and the Tokonami *et al.* (1972) pyrrhotite, and confirms that the Phoenix pyrrhotite was monoclinic 4C pyrrhotite. The space group could not be

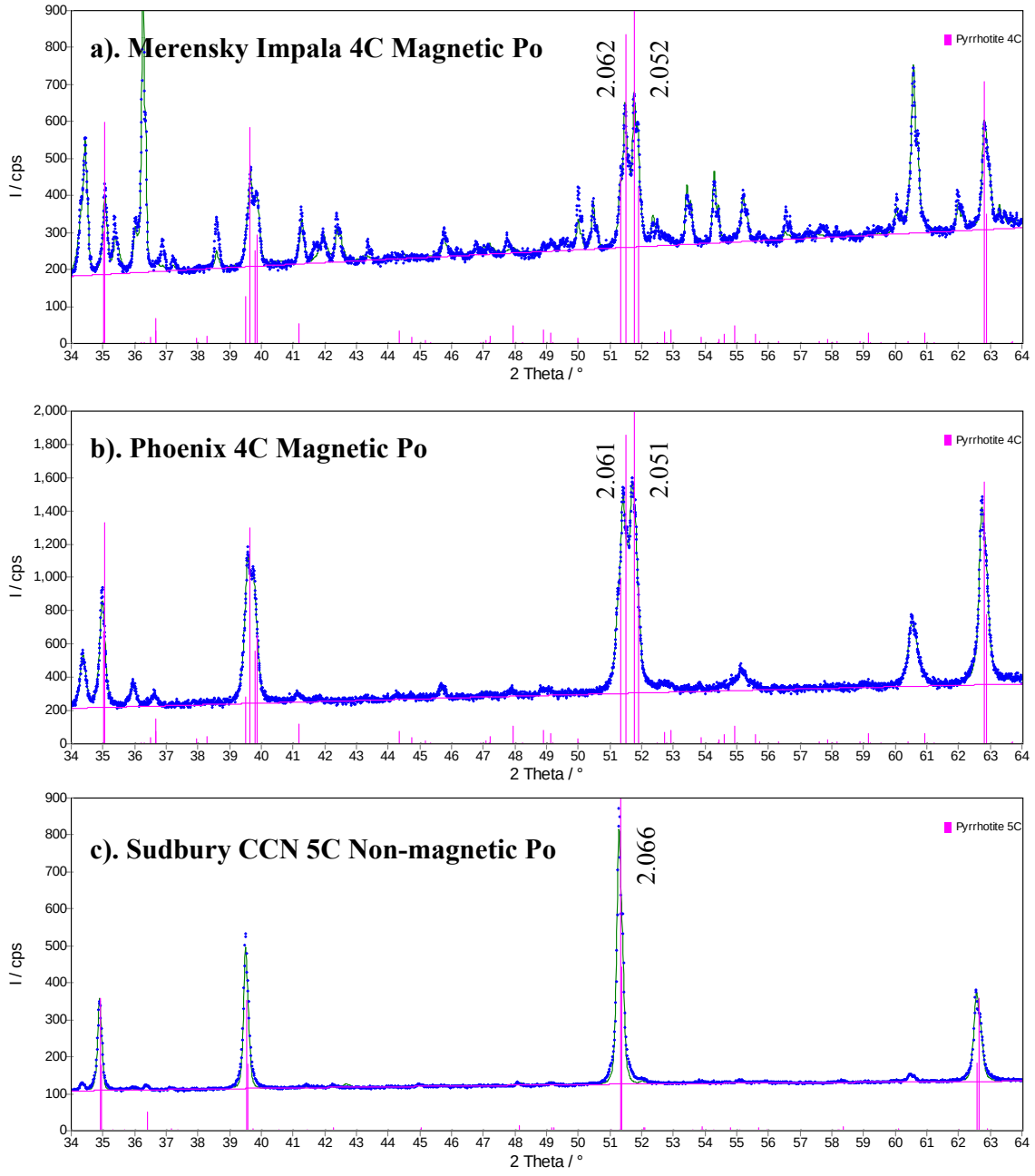

Figure 4.9: Diffractograms from powder XRD analysis of (a) Impala Merensky Reef sample *IMP-1* 4C magnetic pyrrhotite (b) Phoenix 4C magnetic and (c) Sudbury CCN 5C non-magnetic pyrrhotite samples. The peak positions calculated from the reference structures for magnetic pyrrhotite from Powell *et al.* (2004) and non-magnetic pyrrhotite from De Villiers *et al.*(Submitted) are shown in pink, whereas the measured diffractogram is shown in blue. d-spacings of characteristic peaks are given in Å.

unequivocally determined, most likely as a consequence of the poor crystallinity of the specimen analysed. However, since another suitable single crystal could not be found for complete structure analysis, the cell dimensions obtained here are accepted as sufficient evidence to confirm that the Phoenix pyrrhotite is 4C monoclinic pyrrhotite.

The powder XRD diffractogram of the Phoenix magnetic pyrrhotite in figure 4.9b also shows the characteristic doublet for monoclinic 4C pyrrhotite similar to that described in Section 2.2.8 and shown in figure 2.14. The d-spacing obtained for the characteristic monoclinic pyrrhotite doublet was ~ 2.051 and 2.061 Å respectively, and which showed reasonable correlation to the ideal spacing derived from the structure of Powell *et al.* (2004) of 2.056 and 2.066 Å.

4.3.3 Sudbury Pyrrhotite

Preliminary mineralogical characterisation of the Sudbury CCN pyrrhotite showed that it was non-magnetic (Section 4.3) and therefore based on the literature review from Section 2.2, is most likely naturally occurring, NC pyrrhotite. The single crystal XRD results given in table 4.1 show that the c-axis was 28.673 Å in length. This is approximately five times the length of the NiAs unit cell (5.880 Å; Wyckoff, 1963), and hence the Sudbury CCN pyrrhotite was classified as 5C pyrrhotite. The classification of the Sudbury CCN pyrrhotite as 5C pyrrhotite is in agreement with that proposed by Vaughan *et al.* (1971) on their powder diffraction study of pyrrhotite from the Strathcona mine in Sudbury. The cell dimensions for the Sudbury CCN pyrrhotite obtained from single crystal XRD and given in table 4.1 were also similar to that obtained by Morimoto *et al.* (1975b) for 5C pyrrhotite from Kishu mine in Japan. Similarly to the pyrrhotite examined by Morimoto *et al.* (1975b), the Sudbury CCN pyrrhotite displayed orthorhombic symmetry. It should be noted that this is contrary to the common classification of non-magnetic pyrrhotite as “hexagonal” due to the apparent x-ray diffraction symmetry and hexagonal crystal habit (Posfai *et al.*, 2000).

The complete crystal structure of the Sudbury CCN 5C pyrrhotite was subsequently solved by De Villiers *et al.* (Submitted) and will be briefly discussed here. The structure of the Sudbury CCN pyrrhotite is based on sulfur atoms in a hexagonal close packed lattice octahedrally

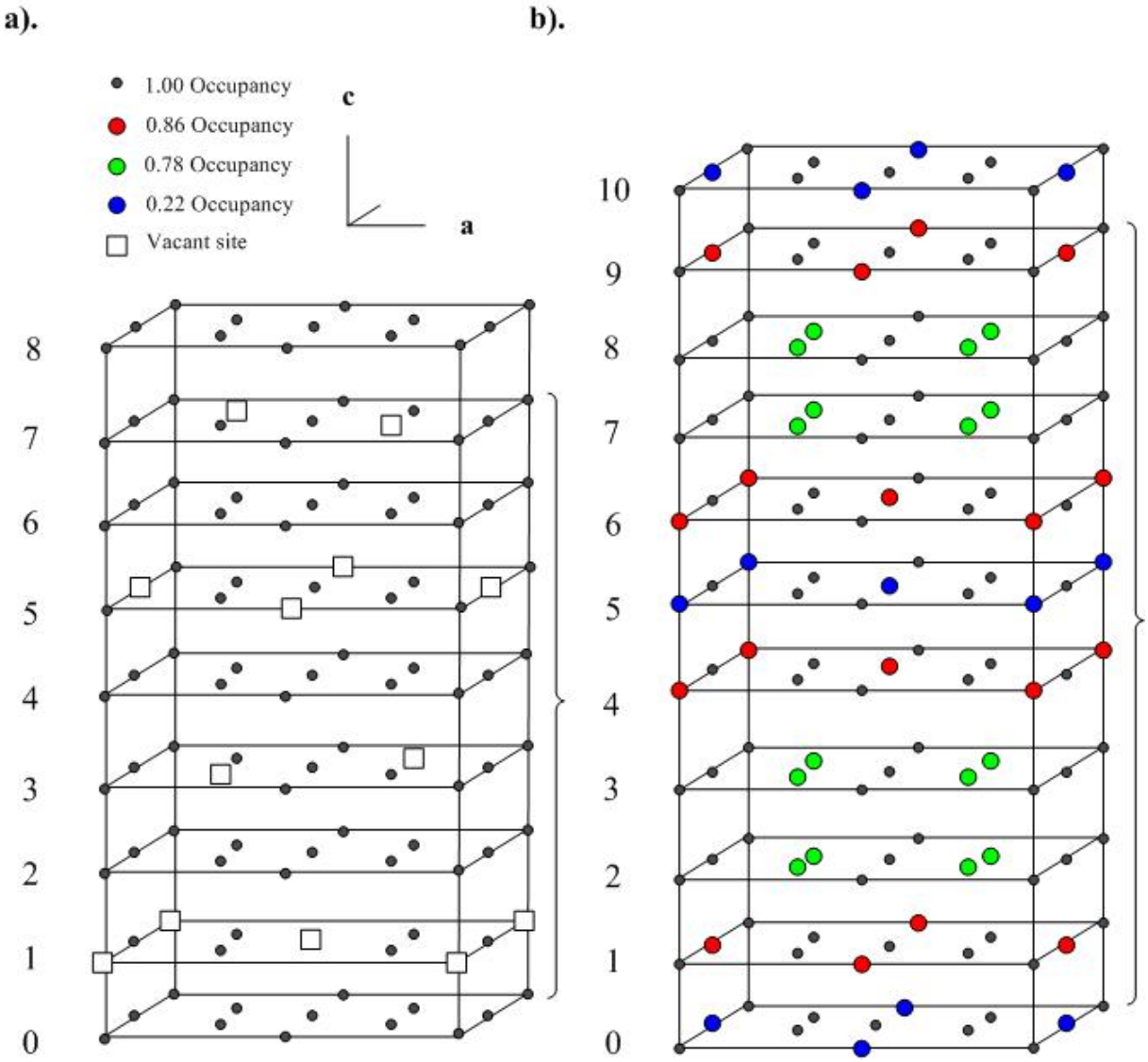

Figure 4.10: Illustration of the vacancy distribution of (a) magnetic 4C pyrrhotite from the structure given in Tokonami *et al.* (1972) and (b) non-magnetic Sudbury CCN 5C pyrrhotite from the structure given in De Villiers *et al.* (Submitted). Sulfur sites are omitted for clarity. Layer 0 represents the origin and the brackets indicate a complete unit cell.

coordinated around the metal atoms. These arrays form a series of layers that are vertically stacked on top of one another as shown in figure 4.10. One of key contributions from De Villiers *et al.* (Submitted) is that unlike the 4C pyrrhotite structures of Tokonami *et al.* (1972) and Powell *et al.* (2004), the 5C pyrrhotite structure contains partially filled iron sites as opposed to completely vacant irons sites. These partially filled iron sites are distributed throughout the entire pyrrhotite structure such that no single layer of the structure is fully

occupied. Rather, every layer consists of a series of partially filled iron sites and hence, the annotation "…FAFBFCFD…" where F denotes a fully occupied layer, and A to D vacancy containing layers (Figure 2.8), and which was used in Section 2.2.5 is not applicable here. Consequently, individual layers are described numerically in figure 4.10. The comparison of the pyrrhotite structures in figure 4.10 is based upon the unconventional F2/d unit cell by Tokonami *et al.* (1972), but which is used since it facilitates comparison of the vacancy ordering.

The vacancy distribution of the 5C Sudbury CCN pyrrhotite illustrated in figure 4.10 shows that in addition to the fully occupied iron sites, layer 1 is comprised of four partially filled iron sites with an occupancy of 0.86. This is overlain by layers 2 and 3 which have four partially filled iron sites with an occupancy of 0.78. This is in turn overlain by layers 4, 5 and 6 whereby the partially occupied sites fall in the same positions, although with an occupancy of 0.86, 0.22 and 0.86, respectively. Layers 7 and 8 are a repeat of layers 2 and 3. Layer 9 is a repeat of layer 1. Layer 10 is repeat of layer 9, although the vacancy of the partially occupied sites is 0.22 instead of 0.86. Based on this ordering of iron site occupancies, the formula for the Sudbury CCN single crystal analysed was $Fe_{8.961}Ni_{0.117}Cu_{0.001}S_{10}$ (De Villiers *et al.*, Submitted).

Some correlation however, exists between the position of the partially filled sites of the 5C pyrrhotite and the vacant sites in the 4C pyrrhotite structure (Figure 4.10). The distribution of partially filled iron sites for the 5C pyrrhotite in layers 1, 9 and 10 is similar to the vacant sites in layer 5 of the 4C pyrrhotite. Similarly, the distribution of the partially filled iron sites for the 5C pyrrhotite in layers 4, 5, and 6 is similar to the vacant sites in layer 1 of the 4C pyrrhotite.

The average occupancy for each layer was calculated on the basis that the occupancy of a layer without any vacant sites is 1 and the occupancy of a layer with 2 vacant sites is 0.75. Based on the monoclinic 4C pyrrhotite structure of Tokonami *et al.* (1972) and Powell *et al.* (2004), an occupancy of 0.75 was obtained for the vacancy layers. This results in a saw tooth pattern when the occupancy is described according to the layer number as in figure 4.11. Similarly, the occupancy of 5C pyrrhotite can be calculated to be 0.968 in layers 1, 4, 6 and 9; 0.893 in layers 2, 3, 7 and 8; and 0.817 in layers 5 and 10. Unlike the saw tooth pattern

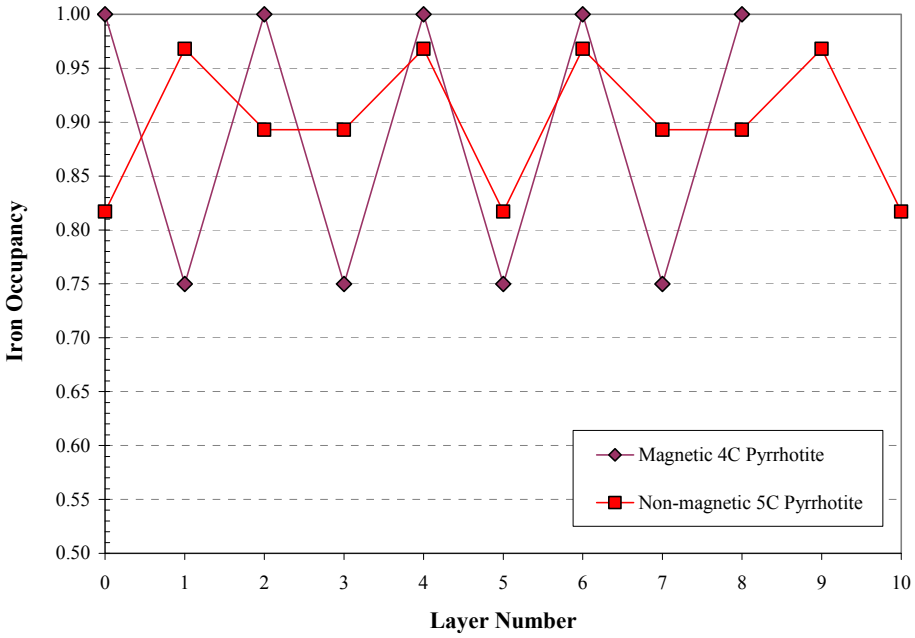

Figure 4.11: Occupancy of iron in the different layers of Sudbury CCN non-magnetic 5C pyrrhotite compared to magnetic 4C pyrrhotite based on the crystal structures from De Villiers *et al.*(Submitted) and Tokonami *et al* .(1972), respectively.

observed for 4C pyrrhotite that varied periodically between alternate layers in figure 4.11, the periodicity for 5C pyrrhotite occurred every five layers.

Based upon the structure obtained from the 5C Sudbury CCN pyrrhotite by De Villiers *et al*, (Submitted), the lines forming the characteristic powder diffraction pattern for 5C pyrrhotite could be calculated. These were compared with the actual powder diffraction pattern obtained for the Sudbury CCN pyrrhotite in figure 4.9c where it is evident that there is good agreement. Figure 4.9c also shows that the powder XRD pattern of the Sudbury CCN pyrrhotite contains a characteristic singlet at d = 2.066 Å. This is similar to the observed and calculated d-spacing for 5C pyrrhotite from Vaughan *et al.* (1971) as well as Carpenter and Desborough (1964).

4.4 Mineral Chemistry

Previous studies on pyrrhotite mineral chemistry have indirectly derived the chemical composition of the pyrrhotite based on the d-spacing of the 102 reflection following the method developed by Arnold and Reichen (1962). Few have examined the inter- and intra-pyrrhotite compositional variation in mineral chemistry for pyrrhotite from various localities and compared it to the ideal composition of Fe_7S_8 (60.4 wt % Fe), Fe_9S_{10} (61.1 wt % Fe), $Fe_{10}S_{11}$ (61.3 wt % Fe) and $Fe_{11}S_{12}$ (61.5 wt % Fe). As such, the following dataset presented here can be considered to be unique in its content, especially since it is based on actual mineral chemistry as opposed to inferred mineral chemistry. The mineral chemistry of pyrrhotite is described first according to locality, then the combined compositions of magnetic and non-magnetic pyrrhotite are compared for the entire pyrrhotite dataset. Individual pyrrhotite analyses are reported in Appendix A.

4.4.1 Merensky Reef Pyrrhotite

Chemical analyses of the Impala Merensky Reef pyrrhotite are illustrated in figure 4.12 where analyses from both samples *IMP-1* and *IMP-2* are shown. The petrographic studies (Section 4.2) showed that sample *IMP-1* consisted of entirely magnetic pyrrhotite, whereas *IMP-2* was comprised of intergrown non-magnetic pyrrhotite and troilite.

Iron contents for all Merensky Reef pyrrhotite occurrences varied between 58.7 and 61.9 wt % with the most iron poor compositions occurring for the magnetic pyrrhotite (Figure 4.12a). The most iron rich pyrrhotite was the non-magnetic Merensky Reef pyrrhotite sample *IMP-2*, although the troilite coexisting with this pyrrhotite was even more iron rich (up to 63.1 wt % Fe; Figure 4.12). Accordingly, the most sulfur rich pyrrhotite was the magnetic Merensky Reef sample *IMP-1* (40.2 wt %) and the most sulfur poor pyrrhotite was the non-magnetic Merensky Reef pyrrhotite (37.4 wt %). The measured sulfur contents of troilite were however, even more depleted in sulfur (36.2 wt %).

Three distinct clusters are apparent when the nickel content of the Impala Merensky Reef pyrrhotite is evaluated as shown in figure 4.12b. Merensky Reef troilite was the most nickel

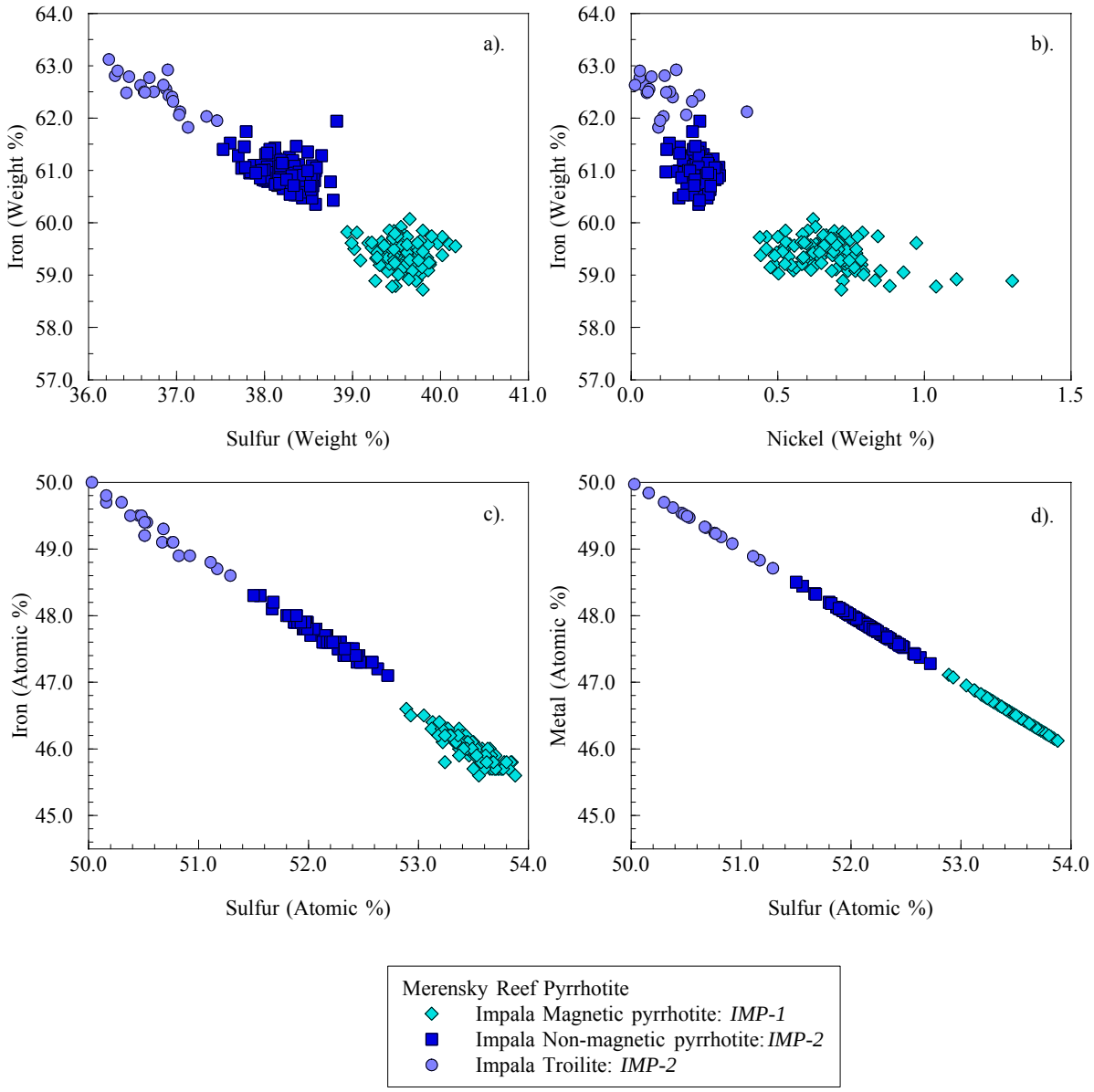

Figure 4.12: Mineral chemistry of Merensky Reef magnetic and non-magnetic pyrrhotite shown as both weight % (a, b) and atomic % (c, d).

poor occurrence (< 0.23 wt % Ni) and the coexisting non-magnetic pyrrhotite in sample *IMP-2* was only slightly more nickel rich (0.11 - 0.30 wt %). Magnetic Merensky Reef pyrrhotite sample *IMP-1* however, was significantly the most nickel rich pyrrhotite of the occurrences investigated here (0.44 – 1.30 wt % Ni).

Atomic iron contents for Impala Merensky Reef troilite varied between 48.6 and 50.0 atomic %, and sulfur varied between 50.0 and 51.3 atomic % (Figure 4.12c). It is noted that the

troilite composition was somewhat more iron poor than would be expected for stoichiometric FeS (~ 50% atomic Fe, 50% atomic S), but it is recognised that this was most likely due to contamination from the coexisting non-magnetic pyrrhotite because of the analytical difficulties associated with analysing such fine grained minerals (< 5 µm). The coexisting non-magnetic pyrrhotite sample *IMP-2*, however, varied between 47.1 and 48.3 % atomic iron, and between 51.4 and 52.7 % atomic sulfur. Magnetic pyrrhotite sample *IMP-1* was distinctly more iron poor (45.5 – 46.6 atomic %) and sulfur rich (52.9 – 53.9 atomic %) than the non-magnetic pyrrhotite.

When the atomic iron is graphed against the atomic sulfur composition of the Merensky Reef pyrrhotite occurrences, a fairly linear, negative correlation is observed (Figure 4.12c), although there is some scatter in terms of atomic iron compositions. When the entire element suite analysed is shown as atomic metal (Fe + Ni + Cu + Co) versus sulfur as in figure 4.12d, it is apparent that this scatter was compensated for by the additional metal cations. However, the compensation was almost entirely due to the nickel composition since the contribution of cobalt and copper to the pyrrhotite chemistry was virtually negligible (Appendix A).

In order to determine the ideal or theoretical composition of the different Merensky Reef pyrrhotite samples, the metal to sulfur ratios were calculated and then the ratio normalised to different ideal sulfur proportions. When normalised to 8 sulfur atoms, the metal / sulfur ratio could be used to examine the variation for a pyrrhotite of ideal composition Fe_7S_8. When normalised to 10 sulfur atoms, the metal / sulfur ratio could be used to examine the variation of pyrrhotite for an ideal composition of Fe_9S_{10} and so forth. The ratios of all the Merensky pyrrhotite occurrences were subsequently examined to determine their ideal composition and the normalised ratio closest to n (for $Fe_{n-1}S_n$ where $n \geq 8$) selected as the ideal. None of the metal / sulfur ratios obtained corresponded to a composition of $Fe_{10}S_{11}$.

By following such a strategy to determine the ideal composition of Impala Merensky Reef pyrrhotite, the compositional variation in terms of the distribution could be examined and the data illustrated in histogram format. It is apparent from the histogram for magnetic Merensky Reef pyrrhotite shown in figure 4.13a that sample *IMP-1* has an ideal composition close to Fe_7S_8. The histogram of the metal / sulfur ratios for magnetic pyrrhotite tends to show a Gaussian distribution and it is noted that the peak of the histogram corresponded with a composition between 6.95 and 7.00 metal cations (34 occurrences) per 8 sulfur anions. The

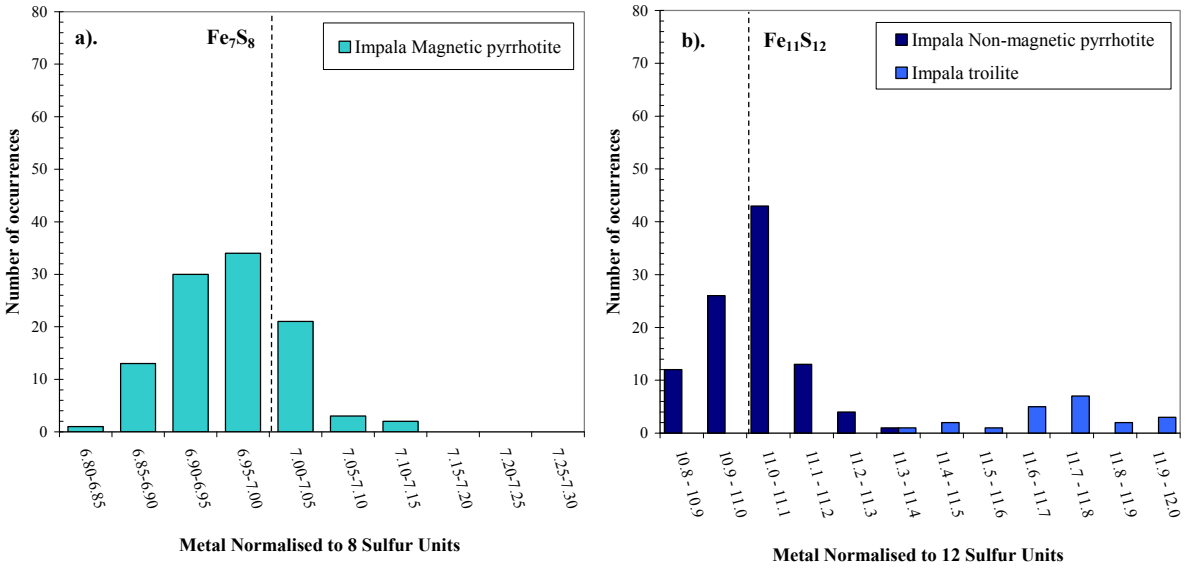

Figure 4.13: Histogram of metal / sulfur ratios normalised to differing sulfur contents for Merensky Reef magnetic (a) and non-magnetic (b) pyrrhotite.

ideal composition obtained for non-magnetic Impala Merensky Reef pyrrhotite sample *IMP-2* (Figure 4.13b) was close to $Fe_{11}S_{12}$ and the most commonly occurring composition was actually slightly more iron rich (43 occurrences in the 11.0 – 11.1 bin) than the ideal.

Based on the mineral chemistry, magnetic pyrrhotite from sample *IMP-1* was classified as Fe_7S_8 which is in agreement with the assignment of sample *IMP-1* pyrrhotite as 4C monoclinic pyrrhotite from the crystallographic studies (Table 4.1). Given that the non-magnetic pyrrhotite is naturally occurring and not synthetic, it could also be assumed that the pyrrhotite falls into the NC superstructure (Table 2.2). From the mineral chemistry, the composition of the non-magnetic pyrrhotite in sample *IMP-2* was determined to be $Fe_{11}S_{12}$. The NC superstructure of pyrrhotite could be linked to its ideal composition using the relationship of Morimoto *et al.* (1970) whereby $Fe_{n-1}S_n$ ($n > 8$). If *n* is even, then the structure is *n*/2C and therefore pyrrhotite from sample *IMP-2* was classified as 6C pyrrhotite. It is also noted that the 6C pyrrhotite from sample *IMP-2* was intergrown with 2C troilite.

Although only 4C magnetic and 6C non-magnetic pyrrhotite were identified in the Merensky Reef samples examined in this study, this is probably not the only occurrence of pyrrhotite in the Merensky Reef. According to Liebenberg (1970), intergrown magnetic and non-magnetic

pyrrhotite are common. Further sampling of pyrrhotite from the Merensky Reef is therefore recommended, in order to confirm the observations of Liebenberg (1970).

4.4.2 Nkomati Pyrrhotite

Iron and sulfur contents of non-magnetic Nkomati pyrrhotite from both the MMZ and MSB illustrated in figure 4.14a are almost identical in composition to each other, and varied from 59.4 to 60.7 wt % iron and between 38.4 and 39.3 wt % sulfur. In contrast, the magnetic pyrrhotite occurrences from the MSB and MMZ show some disparity. Magnetic pyrrhotite from sample *MMZ-4* is compositionally similar to magnetic pyrrhotite from the MSB, both of which were noted to occur in conjunction with non-magnetic pyrrhotite. Magnetic pyrrhotite sample *MMZ-1* from the MMZ however, does not coexist with any other pyrrhotite type and it is this pyrrhotite which is compositionally much more iron poor (58.4 -59.3 wt % Fe) than the other Nkomati magnetic pyrrhotite occurrences (59.1 – 60.2 wt % Fe). In terms of sulfur content, no difference was observed between sample *MMZ-1* and the other magnetic MSB and MMZ (sample *MMZ-4*) pyrrhotite occurrences (39.0 – 39.9 wt % S).

The difference in iron content between the different Nkomati magnetic pyrrhotite occurrences is similarly manifested by the differences in nickel content shown in figure 4.14b. Magnetic MSB and MMZ pyrrhotite (sample *MMZ-4)* coexisting with non-magnetic pyrrhotite was generally more nickel poor (0.26 – 0.67 wt % Ni) than the coexisting non-magnetic MSB and MMZ pyrrhotite (0.55 – 0.90 wt % Ni). Magnetic pyrrhotite sample *MMZ-1* was distinctly more nickel rich (0.66 – 1.20 wt % Ni) than the other pyrrhotite occurrences.

Once the atomic iron and sulfur compositions of the Nkomati pyrrhotite occurrences were calculated it is apparent from figure 4.14c that the different pyrrhotite occurrences have distinctive compositional signatures. Non-magnetic pyrrhotite from both the MSB and MMZ was distinctly more iron rich and sulfur poor than the coexisting magnetic pyrrhotite (46.3 - 47.2 atomic % Fe, 52.3 – 53.1 atomic % S). Although magnetic pyrrhotite sample *MMZ-1* was almost identical in sulfur composition (53.1 – 53.9 atomic % S) to magnetic pyrrhotite

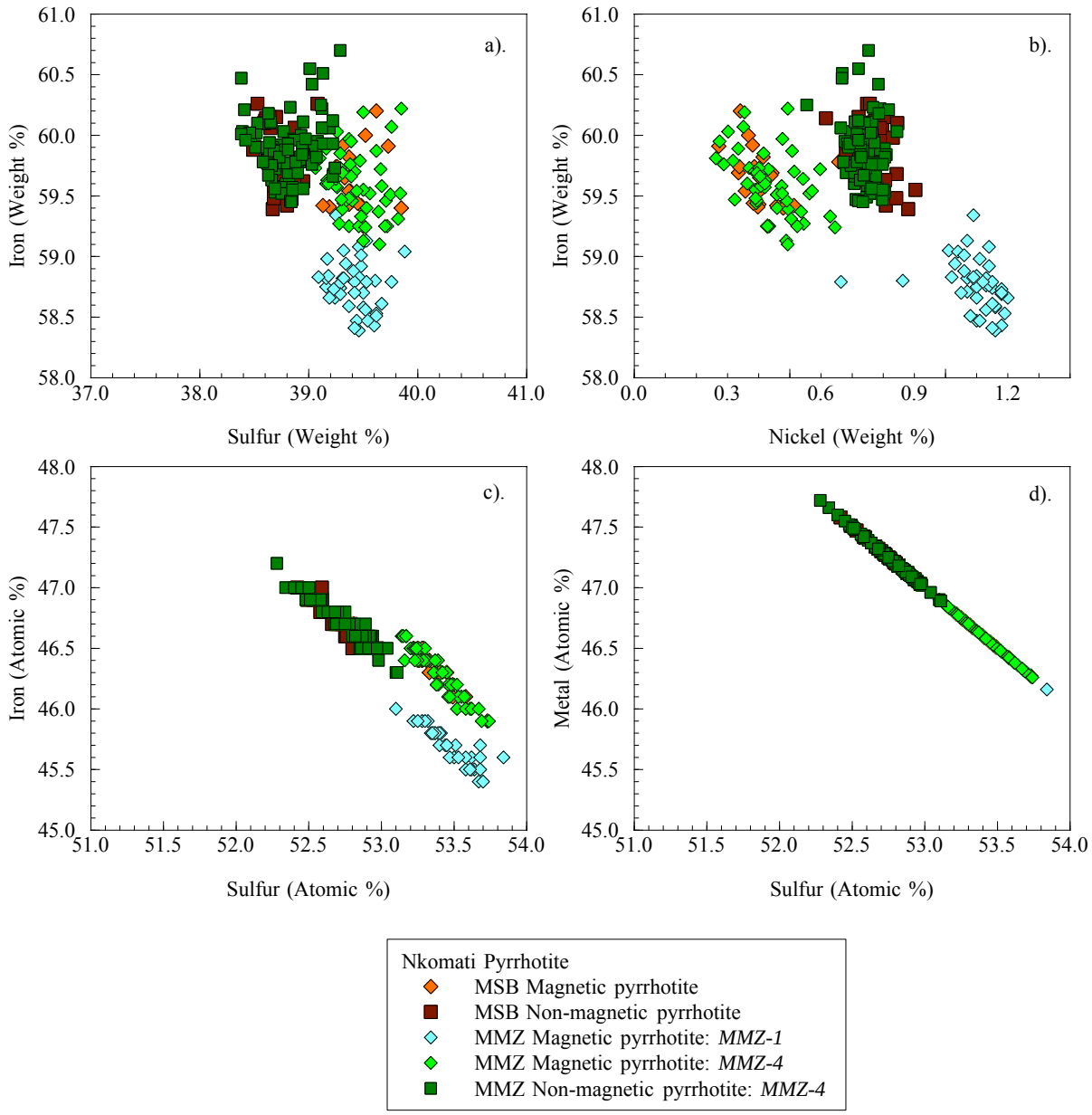

Figure 4.14: Mineral chemistry of Nkomati MSB and MMZ magnetic and non-magnetic pyrrhotite shown as both weight % (a, b) and atomic % (c, d).

sample *MMZ-4* and MSB pyrrhotite, the iron content was quite different (45.4 – 46.0 atomic % Fe). These differences in iron content between the magnetic pyrrhotite occurrences were compensated for by the solid solution substitution of nickel for iron. Therefore, the graph of atomic metal versus atomic sulfur shown in figure 4.14d displays an almost perfect negative correlation for all the Nkomati pyrrhotite occurrences.

Given that all the magnetic pyrrhotite occurrences from Nkomati, including sample *MMZ-1* are similar in composition in terms of their atomic metal composition, the mineral chemistry data could be grouped together and a histogram of the distribution of their metal / sulfur ratios compared. The histogram in figure 4.15a shows that magnetic pyrrhotite from Nkomati has an ideal composition close to Fe_7S_8. Although the most commonly occurring metal / sulfur ratio is 7.00 – 7.05 per 8 sulfur units for the MSB (11 occurrences) and 6.90 – 6.95 per 8 sulfur units for the MMZ (38 occurrences), it is not clear whether they are statistically different or if the difference is due to the small number of Nkomati MSB magnetic pyrrhotite samples analysed. However, for non-magnetic Nkomati pyrrhotite from both the MMZ and MSB, the histogram is similar with an ideal composition close to Fe_9S_{10} (Figure 4.15b). The most commonly occurring metal / sulfur ratio was 8.90 – 8.95 per 10 sulfur units (43 occurrences in total).

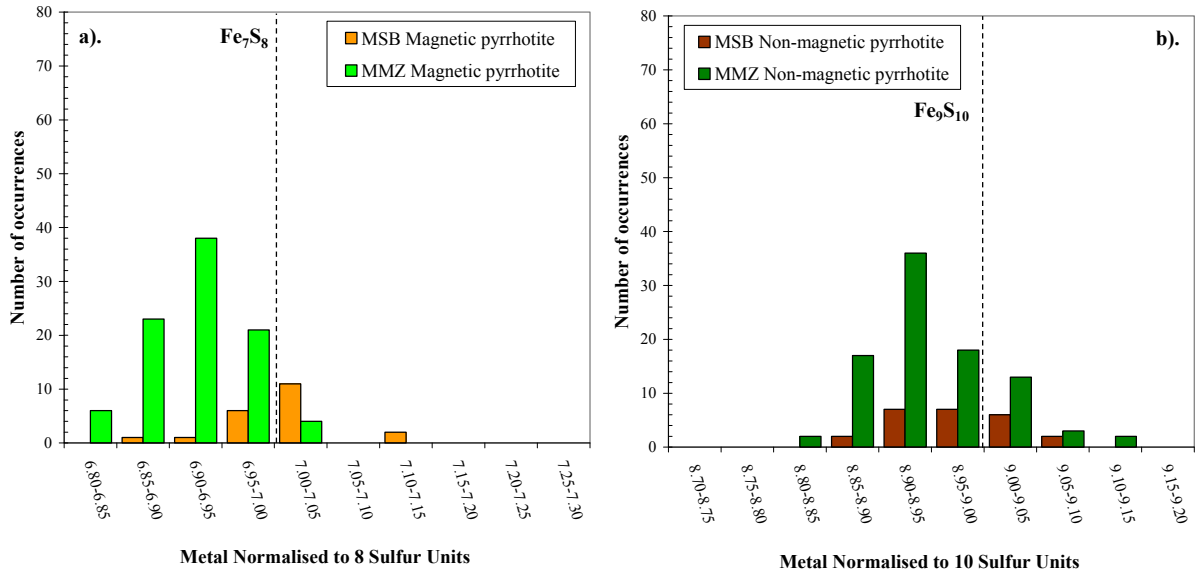

Figure 4.15: Histogram of metal / sulfur ratios normalised to differing sulfur contents for Nkomati magnetic (a) and non-magnetic (b) pyrrhotite.

Based on the mineral chemistry, magnetic Fe_7S_8 and non-magnetic Fe_9S_{10} were identified for the Nkomati pyrrhotite. According to the relationship of Morimoto *et al.* (1970) this corresponds to 4C and 5C pyrrhotite, respectively. It is probable that 5C pyrrhotite observed in the Nkomati MSB and MMZ samples is also orthorhombic, similar to the 5C Sudbury CCN

pyrrhotite sample examined in the crystallographic studies (Section 4.3; De Villiers *et al.*, Submitted).

4.4.3 Phoenix Pyrrhotite

Pyrrhotite from the Phoenix nickel deposit occurred as magnetic pyrrhotite without any coexisting non-magnetic phase. The variation in mineral chemistry of the Phoenix pyrrhotite occurrence is illustrated in figure 4.16. From figure 4.16a, it is evident that Phoenix pyrrhotite shows a broad range in iron composition (57.3 – 60. 0 wt % Fe), but only a relatively narrow range in sulfur content (38.6 – 40.1 wt % S). Similarly to iron in the Phoenix pyrrhotite, nickel also shows a broad range in composition and varied from 0.53 to 2.43 wt % (Figure 4.16b) and which substitutes for iron via solid solution substitution. On the whole, the Phoenix pyrrhotite was relatively enriched in nickel since not only could the nickel budget in the system be accounted for by solid solution nickel but there was also abundant nickel hosted in flame pentlandite. Pyrrhotite from the Phoenix deposit is in fact actively recovered at Tati Nickel mine due to its high solid solution nickel content and abundant pentlandite flames.

The atomic iron content of Phoenix pyrrhotite shown in figure 4.16c displays a broad variation (44.0- 46.5 atomic % Fe), whereas the variation in atomic sulfur is narrow (52.5 – 53.9 atomic % S). Once the contribution from solid solution nickel was accounted for in terms of atomic metal (46.1 – 47.5 atomic % metal), an almost straight and negative correlation occurred between atomic metal and sulfur for the Phoenix pyrrhotite (Figure 4.16d).

Given the very iron deficient nature and the magnetic character of the Phoenix pyrrhotite (Section 4.2), it is likely to have an ideal composition of Fe_7S_8. When the metal / sulfur ratio of Phoenix pyrrhotite was normalised to 8 sulfur atoms, then it is apparent that the most commonly occurring compositions were in the 6.95 – 7.00, 7.00 – 7.05 and 7.05 – 7.10 bins of the histogram illustrated in figure 4.17 (43 occurrences for each bin).

The mineralogical studies of the Phoenix pyrrhotite have therefore shown that it is representative of the archetypal monoclinic 4C pyrrhotite since it was magnetic in character (Section 4.2), showed 4C unit cell dimensions, showed monoclinic symmetry (Section 4.3) and had an ideal composition close to Fe_7S_8.

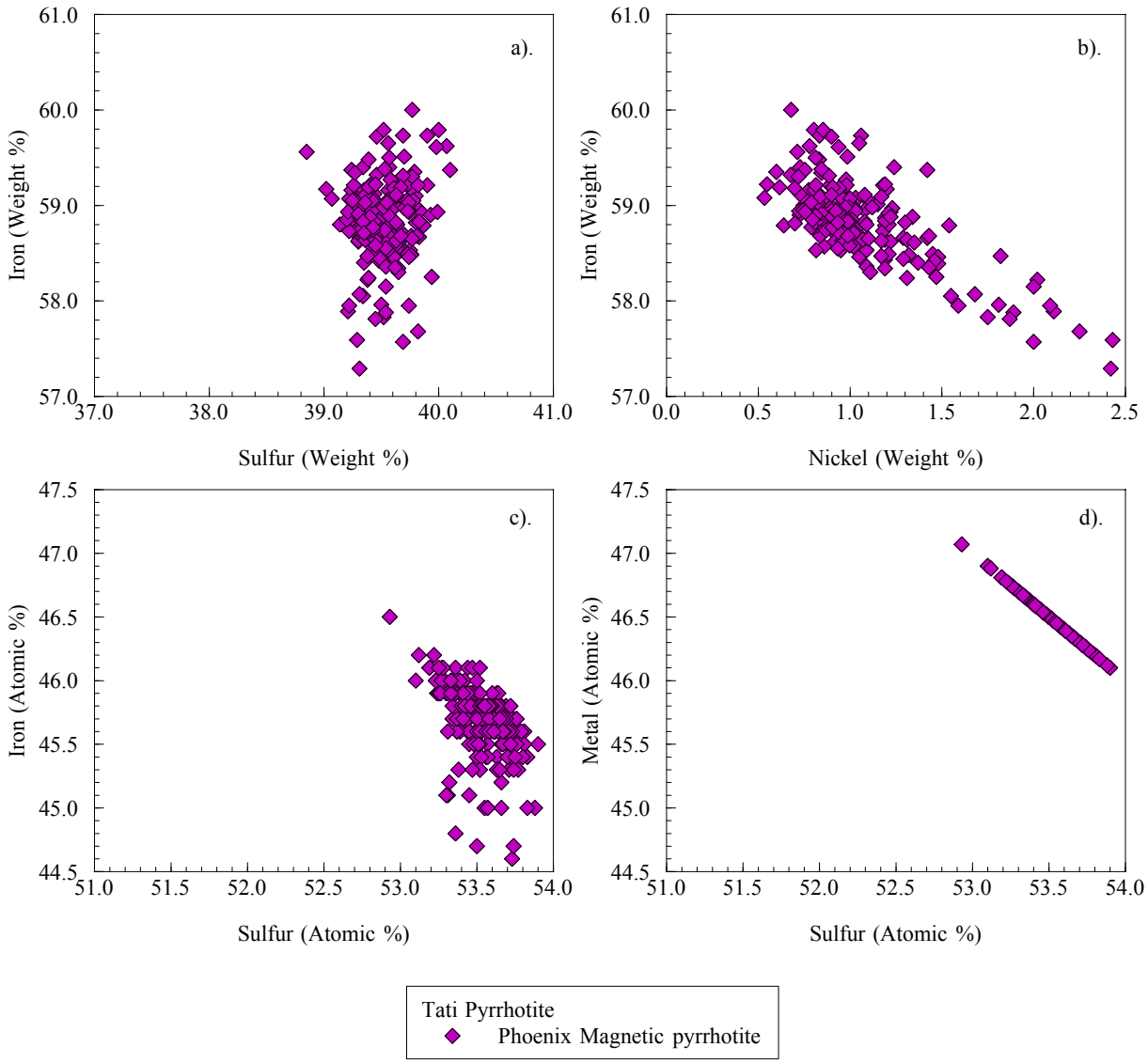

Figure 4.16: Mineral chemistry of Phoenix magnetic pyrrhotite shown as both weight % (a, b) and atomic % (c, d).

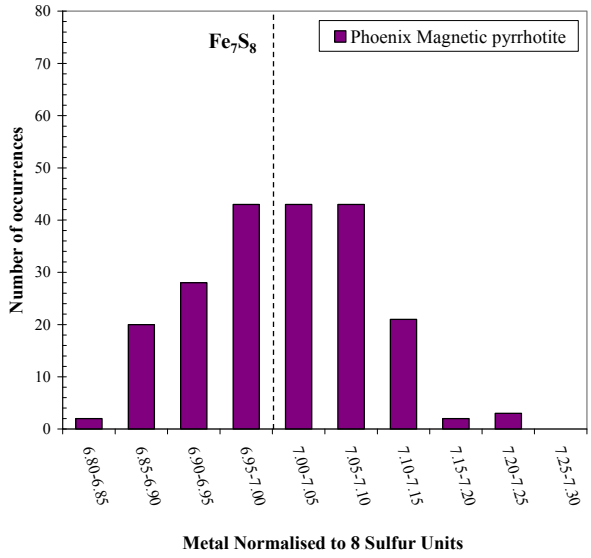

Figure 4.17: Histogram of metal / sulfur ratios normalised to eight sulfur units for Phoenix magnetic pyrrhotite.

4.4.4 Sudbury Pyrrhotite

The petrographic studies showed that both the Sudbury non-magnetic CCN and magnetic Gertrude, Gertrude West pyrrhotite samples were dominated by a single pyrrhotite phase, although very minor proportions of a coexisting secondary phase were recognised on occasion, e.g. magnetic pyrrhotite rims surrounding flame pentlandite in Sudbury CCN pyrrhotite (Figure 4.6c, d). However, for simplicity, the mineral chemistry of each of the pyrrhotite samples is evaluated and interpreted as discrete pyrrhotite occurrences. The variation in mineral chemistry of the Sudbury pyrrhotite occurrences is shown in figure 4.18. The composition of non-magnetic CCN pyrrhotite varied in iron from 59.2 to 60.9 wt % and between 38.2 and 39.5 wt % sulfur (Figure 4.18a). Magnetic Gertrude pyrrhotite was distinctly more iron poor (58.5 – 59.7 wt % Fe) and sulfur rich (38.9 - 40.3 wt % S) than CCN non-magnetic pyrrhotite. Iron and sulfur contents of Gertrude West pyrrhotite (58.4 - 59.8 wt % Fe, 39.2 - 40.1 wt % S) fell into similar compositional fields as Gertrude pyrrhotite. Little difference was observed between the nickel content of the three pyrrhotite localities (Figure 4.18b), although it does appear that the magnetic Gertrude / Gertrude West pyrrhotite were slightly more nickel rich (0.27 – 1.04 wt % Ni) than CCN pyrrhotite (0.40 – 0.98 wt % Ni).

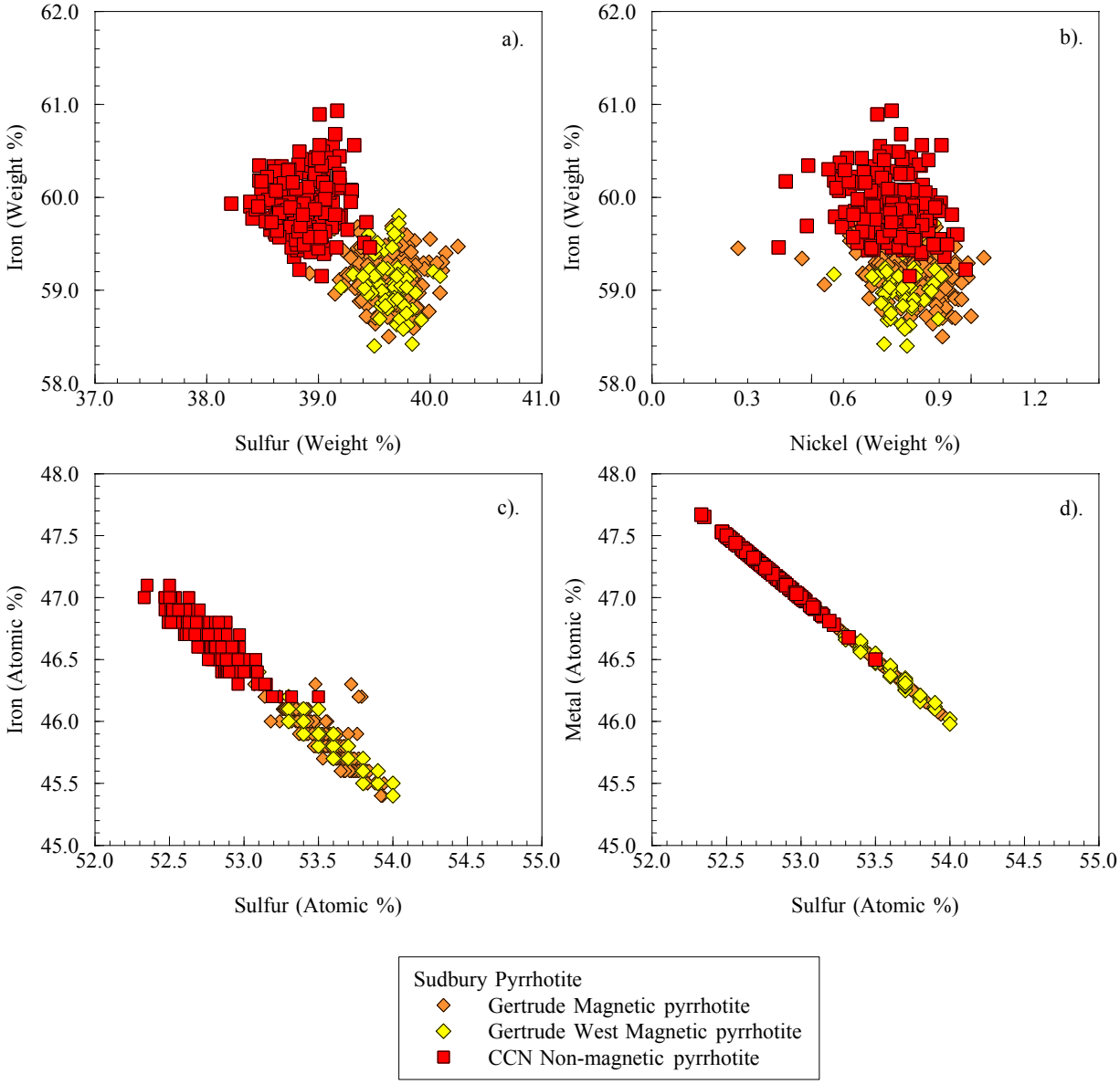

Figure 4.18: Mineral chemistry of Sudbury magnetic Gertrude, Gertrude West and non-magnetic CCN pyrrhotite shown as both weight % (a, b) and atomic % (c, d).

Similarly to the pyrrhotite compositions shown in weight percent, the atomic compositions shown in figure 4.18c for the Sudbury CCN non-magnetic pyrrhotite were more iron rich (46.2 – 47.1 atomic % Fe) and sulfur poor (52.3 – 53.5 atomic % S) than the magnetic Gertrude pyrrhotite (45.4 – 46.3 atomic % Fe, 53.1 – 53.9 atomic % S). The magnetic Gertrude West pyrrhotite showed almost identical atomic iron and sulfur contents to the Gertrude pyrrhotite, confirming their similar origin. Once the additional metal cations were accounted in terms of the contribution of nickel, copper and cobalt as shown in figure 4.18d,

then it is evident that the non-magnetic CCN pyrrhotite varied in atomic metal from 46.5 to 47.7 atomic %, and the magnetic Gertrude / Gertrude West pyrrhotite between 46.0 and 46.9 atomic %.

Due to the iron poor character of the magnetic Gertrude pyrrhotite, the metal / sulfur ratios were normalised to 8 sulfur units according to the ideal composition of magnetic pyrrhotite, Fe_7S_8. It is evident from figure 4.19a that the most frequently occurring metal / sulfur ratio for both Gertrude and Gertrude West magnetic pyrrhotite was between 6.85 and 7.00 Within analytical error this was interpreted to represent a composition close to Fe_7S_8. Gertrude and Gertrude West pyrrhotite were therefore interpreted to represent the archetypal magnetic, monoclinic 4C pyrrhotite. The metal / sulfur ratios corresponding to the non-magnetic CCN pyrrhotite were normalised to 10 sulfur units, as per the ideal composition Fe_9S_{10} (Figure 4.19b). This was consistent with the assignment of Sudbury CCN non-magnetic pyrrhotite as 5C orthorhombic pyrrhotite in the crystallographic studies (Section 4.3). The most frequently occurring metal / sulfur ratio for CCN pyrrhotite was 8.90 – 8.95 per 10 sulfur units (56 occurrences).

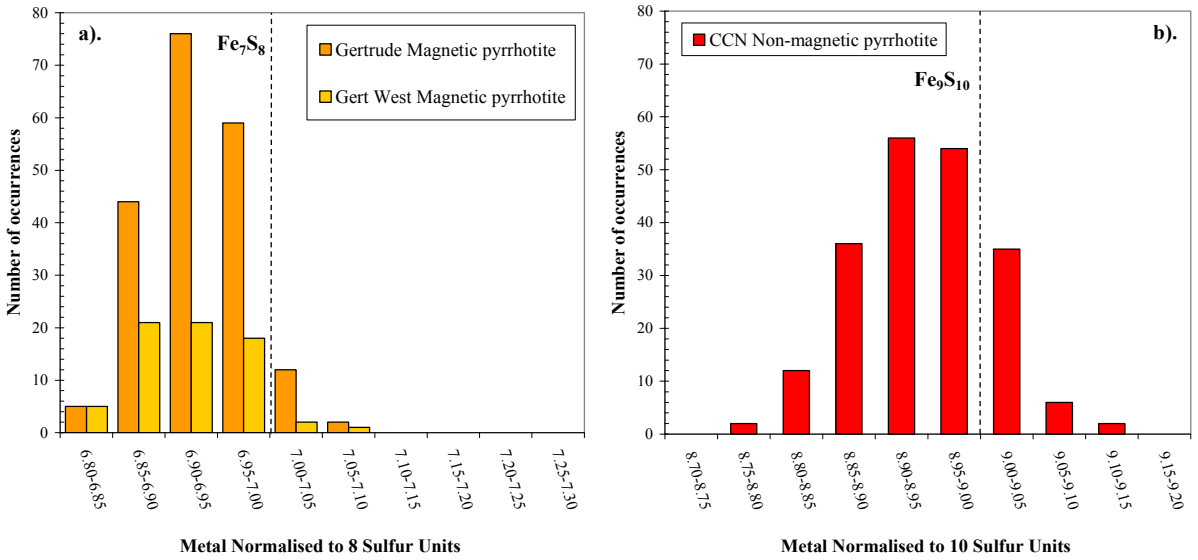

Figure 4.19: Histogram of metal / sulfur ratios normalised to differing sulfur contents for Sudbury magnetic (a) and non-magnetic (b) pyrrhotite.

4.5 Comparison of the Mineral Chemistry of Pyrrhotite Samples

A number of pyrrhotite samples from well-known nickel and platinum group element ore deposits have been characterised in terms of their petrography, crystallography and mineral chemistry. This includes pyrrhotite from magmatic sulfide deposits in South Africa (Merensky Reef, Nkomati) and Canada (Sudbury: Copper Cliff North and Gertrude mines) and from the Tati greenstone belt in Botswana (Phoenix). It is now relevant to compare the compositions of pyrrhotite from these locations in order to develop some general relationships between the pyrrhotite types and explore the compositional variation between the different samples.

Comparison of the iron and nickel contents as illustrated in figure 4.20 showed that a continuum almost exists in terms of the variation in composition of pyrrhotite as a mineral. All non-magnetic pyrrhotite occurrences examined varied in iron between 59.2 and 61.9 wt % and with the more iron rich compositions corresponding to the Impala Merensky Reef 6C $Fe_{11}S_{12}$ pyrrhotite. It is noted that the very iron rich $Fe_{11}S_{12}$ pyrrhotite contained by far the lowest solid solution nickel content (0.30 wt % Ni) and coexisted with 2C troilite (Section 4.2), whereas the nickel content of all the other non-magnetic pyrrhotite occurrences (ie. 5C Fe_9S_{10}) varied between 0.40 and 0.98 wt % (Sudbury CCN, Nkomati MSB and MMZ). The range of nickel contents in non-magnetic Fe_9S_{10} pyrrhotite from this study is significantly broader than the range given by Batt (1972) for non-magnetic Sudbury pyrrhotite and shown in figure 4.20. This may be attributed to the difference in the size of the data sets from this study (> 400 grains) and from the study of Batt (1972; 45 grains). No significant difference in nickel content occurred between non-magnetic pyrrhotite 5C Fe_9S_{10} pyrrhotite which exists as the sole pyrrhotite phase (Sudbury CCN pyrrhotite) or non-magnetic pyrrhotite that coexisted with magnetic 4C Fe_7S_8 pyrrhotite (Non-magnetic Nkomati MSB, MMZ sample *MMZ-4*).

Nickel contents of the more iron poor magnetic 4C Fe_7S_8 pyrrhotite showed a very broad variation from 0.26 to 2.43 wt % nickel. Once again, the variation in nickel contents of magnetic pyrrhotite shown in figure 4.20 are significantly greater than the range given for Sudbury magnetic pyrrhotite by Batt (1972). Only magnetic pyrrhotite that coexists with non-magnetic pyrrhotite (Nkomati MSB and MMZ sample *MMZ-4*) showed some similarity in

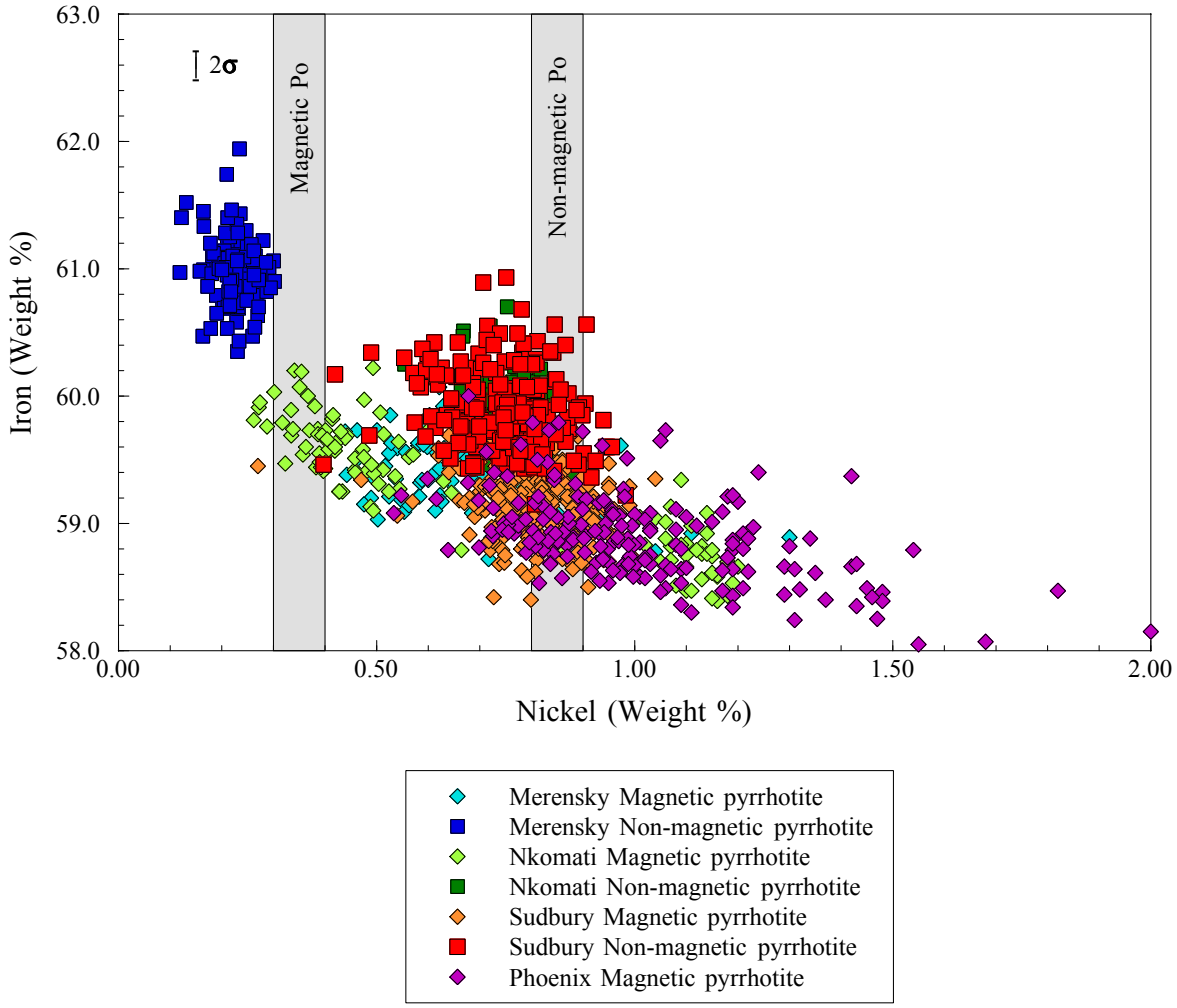

Figure 4.20: Comparison of the wt % iron versus nickel for all magnetic and non-magnetic pyrrhotite occurrences examined in this study. The 2σ standard deviation for iron is shown, whereas the 2σ standard deviation for nickel is too small for representation. The grey bars represent nickel contents for Sudbury pyrrhotite as given by Batt (1972).

nickel content to the values given by Batt (1972), which would be expected given that that the samples examined by Batt (1972) contained intergrown magnetic and non-magnetic pyrrhotite. Under these circumstances, the magnetic pyrrhotite had lower solid solution nickel than the coexisiting non-magnetic pyrrhotite which is in agreement with Batt (1972). The highest solid solution nickel contents for all the pyrrhotite samples in this study were measured for magnetic pyrrhotite that does not coexist with any other pyrrhotite phase (Sudbury Gertrude, Phoenix, Nkomati MMZ sample *MMZ-1*). The Phoenix magnetic pyrrhotite sample however, was notably the most enriched in solid solution nickel of all the pyrrhotite occurrences examined. This confirms that the mineral chemistry of pyrrhotite seems to be correlated with the mineral association.

Atomic iron and sulfur contents for all magnetic and non-magnetic pyrrhotite samples examined and shown in figure 4.21a similarly showed a continuum in terms of the variation in their composition. Non-magnetic pyrrhotite varied between 46.2 and 48.3 atomic % iron and 51.4 and 53.5 atomic % sulfur whereas magnetic pyrrhotite varied between 44.6 and 46.6 atomic % iron and 52.9 and 54.0 atomic % sulfur. Given the degree of overlap in terms of atomic iron or sulfur contents, consideration of both parameters is needed on an x-y diagram to recognise discreet compositional fields of pyrrhotite. On this basis, three groupings in pyrrhotite composition corresponding to magnetic 4C Fe_7S_8, non-magnetic 5C Fe_9S_{10} and non-magnetic 6C $Fe_{11}S_{12}$ can be recognised in figure 4.21a.

For a given sulfur content it also evident that the variation in atomic iron for non-magnetic 6C $Fe_{11}S_{12}$ (~ 0.2 atomic % Fe) was less than for non-magnetic 5C Fe_9S_{10} (~ 0.3 atomic % Fe), and which was even less than for magnetic 4C Fe_7S_8 (~ 0.8 atomic % Fe). This variation in atomic iron was compensated for by other metal cations (i.e. nickel) and when illustrated as the variation of atomic metal versus sulfur in figure 4.21b, an almost perfect negative correlation is observed. The continuum in terms of atomic sulfur contents indicates that the pyrrhotite structure as a whole must be sufficiently flexible that it can accommodate virtually any sulfur content between 51.4 and 53.9 atomic % sulfur.

This continuum observed in terms of pyrrhotite compositional variation was also manifested in the atomic metal / sulfur ratio of pyrrhotite shown in figure 4.22. Pyrrhotite compositions with the lowest metal / sulfur ratio corresponded to the magnetic pyrrhotite occurrences examined in this study, namely the Nkomati MSB and MMZ, Merensky Reef, Phoenix and Sudbury Gertrude and Gertrude West pyrrhotite samples. The variation in metal / sulfur ratio was observed to be broader (Atomic Metal / Sulfur = 0.851 – 0.889) than the ideal for pyrrhotite of composition 4C Fe_7S_8 (Atomic Metal / Sulfur = 0.875). Non-magnetic pyrrhotite of ideal composition 5C Fe_9S_{10} (Sudbury CCN, Nkomati MSB and MMZ) also showed a significantly broader atomic metal / sulfur ratio (0.869 – 0.913) than the ideal (Atomic Metal / Sulfur = 0.900). The highest atomic metal / sulfur ratios occurred for the very iron rich Impala Merensky Reef pyrrhotite (Atomic Metal / Sulfur = 0.897 – 0.942) of ideal composition 6C $Fe_{11}S_{12}$ (Atomic Metal / Sulfur ratio = 0.917).

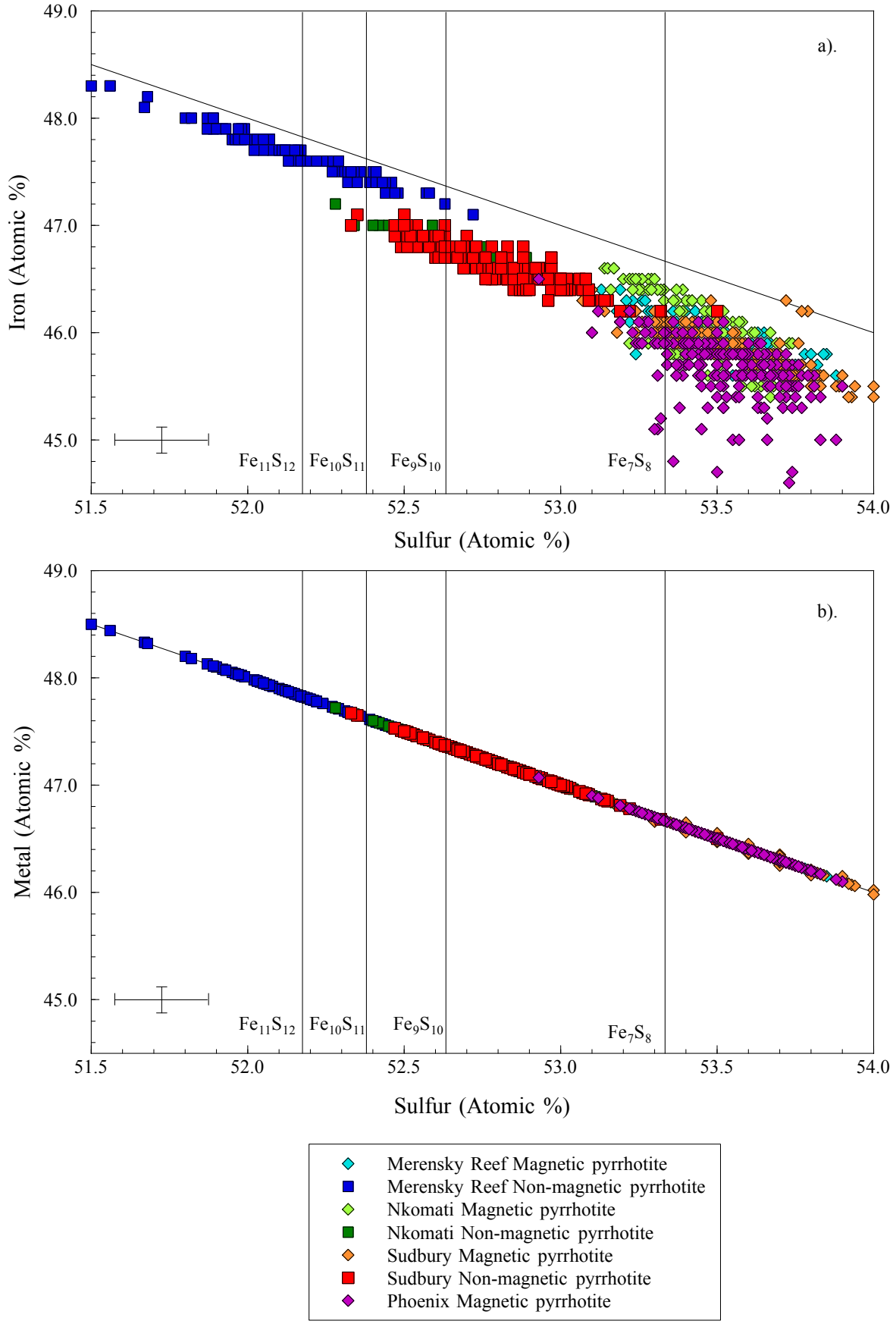

Figure 4.21: Comparison of the atomic % iron (a) and metal (b) versus sulfur for all magnetic and non-magnetic pyrrhotite occurrences examined in this study. The 2σ standard deviation is also shown.

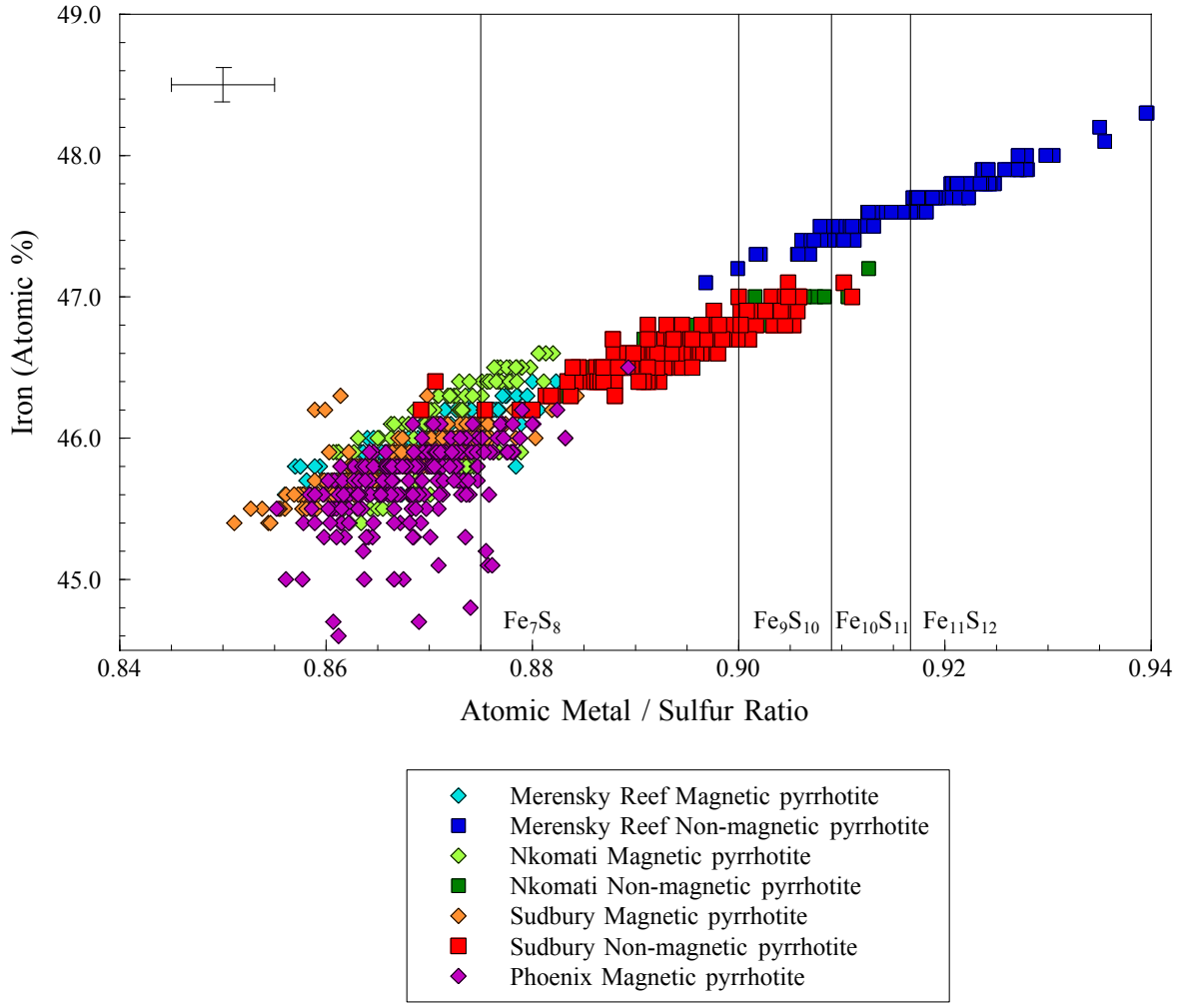

Figure 4.22: Comparison of the atomic % iron versus metal to sulfur ratio for all magnetic and non-magnetic pyrrhotite occurrences examined in this study. The 2σ standard deviation is also shown.

4.7 Key Findings

Key features noted with respect to the mineralogy of pyrrhotite from selected nickel and platinum group element ore deposits were as follows:

Pyrrhotite was the most common sulfide mineral in all of the occurrences examined and with sulfide mineralisation occurring in a variety of textures from massive, semi-massive, net-textured to disseminated. Pyrrhotite was generally fairly coarse-grained, showed well-developed anisotropism, occasional twinning and intergrowth textures to other sulphide minerals characteristic of crystallisation from the MSS. Pentlandite showed a strong association to pyrrhotite and occurred in both granular and flame pentlandite form. Other minerals present in the samples examined included chalcopyrite, pyrite and magnetite in varying proportions.

Application of the magnetic colloid to the pyrrhotite samples revealed the presence of samples that consisted of solely magnetic pyrrhotite, solely non-magnetic pyrrhotite, and intergrowths of magnetic and non-magnetic pyrrhotite. A variety of intergrowth textures between magnetic and non-magnetic pyrrhotite phases that included magnetic pyrrhotite lamellae hosted by non-magnetic pyrrhotite, thickness zonation, box work textures, composite lamellae and magnetic pyrrhotite rims surrounding crystallographically controlled flame pentlandite exsolution were all noted. Very fine grained troilite lamellae intergrown with non-magnetic pyrrhotite were also recognised in the Merensky Reef pyrrhotite sample.

The crystallographic studies showed that both the magnetic Impala Merensky sample *IMP-1* and Phoenix pyrrhotite samples were monoclinic 4C pyrrhotite whereas the non-magnetic Sudbury CCN pyrrhotite was orthorhombic 5C pyrrhotite. The crystal structure solution of the Sudbury CCN pyrrhotite was shown to consist of a series of iron layers that were vertically stacked. Each layer consisted of a series of fully occupied as well as partially occupied iron sites in contrast to the classic structure of 4C pyrrhotite that is comprised of a series of alternating fully occupied layers with vacancy containing layers.

The composition of magnetic pyrrhotite was shown to be more sulfur rich (52.9 - 54.0 atomic % S) and iron deficient (44.6 - 46.6 atomic % Fe) than non-magnetic pyrrhotite (51.4 and 53.5 atomic % S; 46.2 - 48.3 atomic % Fe). Three compositional groups of pyrrhotite were observed correlating to magnetic 4C Fe_7S_8, non-magnetic 5C Fe_9S_{10} and non-magnetic 6C $Fe_{11}S_{12}$. Non-magnetic 6C $Fe_{11}S_{12}$ pyrrhotite was intergrown with 2C FeS.

Nickel was determined to be the main trace element impurity in the pyrrhotite structure. Non-magnetic 6C $Fe_{11}S_{12}$ pyrrhotite was less nickel rich (0.22 ± 0.07 wt %) relative to non-magnetic 5C Fe_9S_{10} pyrrhotite (0.75 ± 0.19 wt %). Magnetic 4C Fe_7S_8 pyrrhotite coexisting with non-magnetic 5C Fe_9S_{10} pyrrhotite typically had a lower nickel content (0.43 ± 0.18 wt %) than the non-magnetic phase (0.75 ± 0.10 wt %). The highest solid solution nickel contents were obtained for magnetic pyrrhotite with no coexisting non-magnetic phase (> 0.82 wt %).